

# **The Effects of Topography on Seismic Motion of the 2010 Mw 7.0 Haiti Earthquake and Associated Damages.**

RUPERT GREEN

March, 2018

SUPERVISORS:

Prof. Dr. M. van der Meijde

Prof. Dr. N. Kerle



# The Effects of Topography on Seismic Motion of the 2010 Mw 7.0 Haiti Earthquake and Associated Damages

RUPERT GREEN

Enschede, The Netherlands, March, 2018

Thesis submitted to the Faculty of Geo-Information Science and Earth Observation of the University of Twente in partial fulfilment of the requirements for the degree of Master of Science in Geo-information Science and Earth Observation.

Specialization: Applied Earth Sciences

**SUPERVISORS:**

Prof. Dr. M. van der Meijde

Prof. Dr. N. Kerle

**THESIS ASSESSMENT BOARD:**

Prof. Dr. F.D. van der Meer (Chair)]

Prof. Dr. Christine Thomas, External Examiner, University of Münster



#### DISCLAIMER

This document describes work undertaken as part of a programme of study at the Faculty of Geo-Information Science and Earth Observation of the University of Twente. All views and opinions expressed therein remain the sole responsibility of the author, and do not necessarily represent those of the Faculty.

## ABSTRACT

The 2010 Mw 7.0 Haiti earthquake had cause significant damage across Haiti and generated numerous landslides. There was substantial damage to the infrastructure in the capital Port-au-Prince. Being located at the foot hill of Massif de la Sella, there was spatial bias in the distribution of damaged buildings. Spectral Element Method was adopted to conduct a numerical simulation to investigate the effects of seismic motion on the 2010 Haiti earthquake. A DEM derived 3D model with topography surface included was used with SEM to simulate the effects of topography. Using a mesh resolution of 180m, the complex terrain was captured and the effects of topography simulated. The simulated result was compared with observed and documented landslides and damaged buildings. Using a combination of building damage density and topography induced amplification and insight of the damage pattern was obtained. The damage pattern may be due to combination of topography induced amplification and building quality. The relationship between topography amplification and landslides was was very complex and topography amplification could not explain the landslide pattern indicating that other factors may influence the distribution.

## ACKNOWLEDGEMENTS

Thanks to the Almighty God who gave me the knowledge, His grace and blessings to finish this work.

Many thanks to the ITC scholarship providers who help financed my MSc study and without their scholarship, I could not come to ITC for study.

I express my gratitude my two supervisors Professor Dr. M. van der Meijde, Professor Dr. N. Kerle, who provide much guidance for this study.

I am eternally grateful to my employer, The University of the West Indies for allowing me to come to the Netherlands for study. My thanks goes out to my fellow classmate and colleagues as the teachers of the department of Earth System Analysis.

Finally, I would like to thank my parents for their undying support as well as my friends in the Caribbean for their warm greeting during the cold.

# TABLE OF CONTENTS

---

1	Introduction.....	1
1.1	Background.....	1
1.2	Research Problem.....	2
1.3	General Objective.....	3
2	Surface Topography effects on Seismic Ground motion: A review.....	5
2.1	Studies on the effects of surface topography of the seismic motion.....	5
2.2	Effects Topography on Seismic Induced Ground Motion – SEM Applications.....	7
3	2010 $M_w$ 7.0 Haiti Earthquake: Review.....	9
3.1	Seismo-tectonic setting of Hispaniola.....	9
3.2	Earthquake-induced ground motion: Site response.....	11
3.3	Earthquake-induced - Building Damage Assessment.....	12
4	Methodology.....	15
4.1	First stage: Simulation of the earthquake.....	15
4.2	Second stage: Comparison of simulation and observations.....	20
5	Results.....	25
5.1	The Effects of Surface Topography on Seismic Ground Motion.....	25
5.2	Relation Between Landslides and Seismic Amplification.....	32
6.	Discussion.....	43
7.	Conclusion.....	47

# LIST OF FIGURES

---

Figure 3.1: Seismo-tectonic setting of Hispaniola [ .....	10
Figure 3.2: The fault mechanism for the Mw 7.0 earthquake 2010.....	11
Figure 3.3 showing the damage assessment extent from Léogâne to Cul-De-Sac basin.....	13
Figure 4.1: The geometry of hexagonal finite.....	17
Figure 4.2: Mapping to reference section.....	18
Figure 4.3: Showing the methodological flowchart for ground motion modelling.....	19
Figure 4.4: Landslide.....	21
Figure 4.5: Distribution of Building Inventory (.....	23
Figure 4.6: European Macroseismic scale 1998 (EMS 98) .....	23
Figure 5.1 : Spectral Element Mesh.....	25
Figure 5.2 The major element size for 180m with topography .....	26
Figure 5.3: The major element size for 180m without topography.....	26
Figure 5.4: Peak Ground Displacement .....	29
Figure 5.5: Snapshots at different time steps for the Z-component displacement wavefield o .....	30
Figure 5.6: The location of the seismic station in Presa de Sabaneta, Dominican Republic. ....	30
Figure 5.7: Comparision of the artificial seismograms, .....	31
Figure 5.8: Comparison of the observed (SDDR) signal with the signal from statio .....	31
Figure 5.9: Landslides (red dots) located within study area along with the CMT.....	32
Figure 5.10: Distribution of Landslide with respect to CMT location in a rose diagram.....	33
Figure 5.11: Box plot of the landslide aspect against the PGD amplification.....	34
Figure 5.12: Landslide density map with density.....	34
Figure 5.13: Landslide Density with respect to PGD amplification.. ..	35
Figure 5.14: PGD amplification model with Hotel Montana .....	36
Figure 5.15: Distribution of UNOSAT inventory .....	37
Figure 5.16: The spatial distribution of no/moderate damaged buildingsn .....	38
Figure 5.17: The spatial distribution of heavy damaged buildings with respect to PGD amplification .....	39
Figure 5.18: Boxplot of the amplification values .....	40
Figure 5.19: Total Building Map .....	40
Figure 5.20: Damage Density overlain on PGA Amplification map .....	41
Figure 5.21: The damage density with respect to categorised PGD amplification.....	41
Figure 6.1: PGD amplification model:.....	44
Figure 6.2: Profile.....	44
Figure 6.3: PGD amplification landslide density map.....	45
Figure 6.4.: Profile A:B.....	46

## LIST OF TABLES

---

Table 4.1: PGD Amplification Classification.....	22
Table 4.2: Damage Grade for the Building Inventory.....	23
Table 5.1: Mesh (180m) properties for seismic simulation.....	27
Table 5.2: Landslides and Amplification Maps with classified amplification.....	32
Table 5.3: Number of no/moderate damaged Buildings with respect to classified PGD amplification .....	37
Table 5.4: Number of heavy damaged buildings with respect to classified PGD amplification .....	38
Table 6.1: Mesh design for 270m and 180m resolution .....	43



# 1 INTRODUCTION

## 1.1 Background

High magnitude earthquakes have resulted in significant losses regarding human life and infrastructure in the western hemisphere. On January 12th, 2010, one of the most impoverished country in the western hemisphere, the Republic of Haiti, was devastated by an earthquake (Mw 7.0). As a result of this event, there was significant damage to infrastructure in the capital, Port-au-Prince as well as generating at a minimum of 4490 landslides in the surrounding hills (Gorum et al., 2013). In fact, this event resulted in a death toll of over 217,000 individuals (Eberhard et al., 2010), while over “97,294 residential structures destroyed and 188,383 damaged beyond repair” (Assimaki & Jeong, 2013), making this a major disaster. Furthermore, the event was estimated to cost the country between US\$7.9 to US\$13.9 billion (Cavallo et al., 2010). Thus, devastating an already economically challenged nation. Hence Haiti was in need of global assistance for disaster relief and recovery. As numerous reconstruction works have occurred in Haiti, an analysis by Symithe & Calais (2016) has indicated that another earthquake of similar magnitude is being projected to occur. Considering such possibilities of a future earthquake, it is essential to have an understanding of how seismic waves propagate within this region. To achieve such an understanding, the observed and documented impact of 2010 Haiti earthquake provides much-needed data to understand the seismic response within the region.

To develop a better understanding of the seismic response, the influence of topography should be included in the analysis along with those effects due to sediments. As seismic waves propagate through the earth, they interact with topography and the sediments which may result in the (de-)amplification of the seismic signal (Hartzell et al., 2017; Kouteva-Guentcheva et al., 2009). Sediments are well known to amplify the seismic waves as in the classic case of Mexico City in 1985 (Çelebi, 1991). There was severe destruction within the city which was attributed to sediments induced amplification from Michoacán earthquake (Mw 8.0) whose epicentre was 400km away (Campillo et al., 1989). Even though the role sediments in seismic wave amplification is well understood, numerical simulations are used to provide greater insight. However, the effects of topography on seismic motion are not well established. By having a closer look at the role of topography, Favretto-Cristini et al. (2014) indicated that 3D work is necessary to model topographic features and effects on wave motion. Studies by Ashrafuzzaman (2017) and Khan et al. (2016) have shown that inclusion of 3D topographic models in site response models provided a more accurate way to simulate seismic induced ground motion. Furthermore, topographic structures surrounding sedimentary basins may result in multiple reflection of seismic waves into the basin thus increasing the duration of shaking (Lee et al., 2008; Lee et al., 2009) or actually deflect seismic energy and thereby decreasing the effect of the earthquake (Ashrafuzzaman & MD, 2017).

As seismic waves interact with the earth's surface, the response at each site will vary. These site responses are categorised either as effects on the ground such as earthquake-induced landslides or impact on superstructures such as earthquake-induced building damages.

Earthquake-induced landslides are characterised by elements of the earthquake characteristic, distance from the earthquake, geology and topography. While the relationship between landslides with ground shaking is the focus of numerous studies such as Meunier et al., (2007), little attention has been made between landslides and topographic de/amplification such as in Meunier et al. (2008). Furthermore, even when topographical amplification is included in these studies, the primary focus is on an individual topographical feature such as single hillslope to understand slope instability (e.g. Del Gaudio & Wasowski, 2007). However, the spatial variation of landslides and topographic amplification on a regional scale is still understudied.

The earthquake-induced building damages are a result of a combination of earthquake characteristics, distance from the earthquake, topographic and sediment induced amplification, geology and building characteristics. By examining earthquake-induced building damages in Port-au Prince and surrounding communities, there were high levels of complexity in damage pattern due to the low quality of construction and site effects (Hough et al., 2012; Molina et al., 2014; Torres et al., 2016). However, in several hillslope locations, a pattern of increase in the intensity of building damage or the degree of damage was observed as one move toward the top of the hill from the base. This high degree of damage on the hilltop was exemplified by the destruction of Hotel Montana; the luxury hotel located at Bourdon, Port-au-Prince (Rathje et al., 2011). The level of damage to Hotel Montana was ascribed to be a result of topographic amplification. However, Assimaki and Jeong (2013) had indicated that soil and topography played a role in damage to the Hotel Montana. earthquake, Hough et al. (2010, p.781) stated that little work had been done to evaluate the "nonlinearity of topography amplification." Furthermore, Hough et al. indicated that topographic amplification along a steep, narrow ridge might be more important than amplification from a shallow sedimentary layer. The questions of the role of topography in amplifying or de-amplifying seismic waves in the Haitian context is not well-established nor is there an established correlation with the site response to the modified ground motion. This research tries to explore the role of topography in modifying seismic motion and relate it to the site response, by seeing if the pattern of landslides or building damages can be explained by the modelled ground motion.

## **1.2 Research Problem**

The 2010 Haitian earthquake resulted in significant damage in the Cul-de-Sac basin and generated landslides in the surrounding hills. To develop an understanding of the site response to this earthquake, an examination of ground motion characteristics is necessary. The lack of accelerometers and no surface ruptures make characterising the ground motion and contributing faults of this earthquake very problematic. However, the maximum release point, and the centroid moment tensor (CMT) characteristics provide a means of characterising the earthquake. As the CMT was located offshore, the seismic energy will interact with surface

topography below the sea level as it propagates towards Port au Prince and surrounding hills and then interact with surface topography above the sea level. This interaction of seismic waves and topography results in a complex pattern of de/amplified seismic motion. Therefore, to understand this complex interaction of seismic waves and topography the inclusion of a realistic topography is required in the analysis.

The complex interaction of seismic wave with topography may provide an insight into to the complex site response pattern for both earthquake-induced landslides and damaged buildings. Having an integrated understanding of the complex relationship between seismic energy with topography and associated damages is essential for both local engineers and planners as well as international reconstruction aid agencies especially in the Haitian context. This research provides the scientific evidence required for improvement for local building codes, engineering guidelines for the construction industry and sustainable urban zoning.

### **1.3 General Objective**

The general objective of this study is to determine the effect of topography on seismic motion of the Haitian earthquake (Mw 7.0), 2010 and associated earthquake-induced damages.

To achieve the general objective, two specific objectives are established along with four research questions.

#### **1.3.1 Specific Objectives and Research Question:**

A. To investigate the spatial variation of seismic motion for Haiti, 2010 earthquake (Mw 7.0).

1. What are the spatial variations of seismic motion and how is it amplified or de-amplified by topography in the study area?
2. What are effect of the different resolutions of the topographic model on the seismic motion amplification model for the study area?

B. To correlate the spatial variation in seismic motion and the occurrence of damages.

3. What is the spatial relationship between earthquake-induced landslides and amplification in the study area?
4. How well do the earthquake-induced buildings damage patterns relates to de/amplification seismic motion in the Cul-de-Sac basin?



## 2 SURFACE TOPOGRAPHY EFFECTS ON SEISMIC GROUND MOTION: A REVIEW

This chapter presents a review of various ways in which the effects of topography on seismic ground motion have been studied. An outline of the reasons for each category as well as the limitation associated with each. The chapter also provides a defense for the selecting Spectral Element Method (SEM) in this research by outlining studies that used SEM in studying effects of topography on seismic ground motions.

### 2.1 Studies on the effects of surface topography of the seismic motion

Seismic waves interaction with earth's surface tends to be modified by the irregularity of the surface (Snieder, 1986). Modification occurs as seismic waves are being refocused, diffracted and scattered by the earth's surface (Poursartip et al., 2017). Various studies have investigated the effects of surface topography on the seismic motion as a means of gaining an insight on the seismic response of regions with topographical irregularities. Studies on the effects of surface topography on the seismic motion are mainly divided in four categories: observations after an earthquake; analytical solution using simple geometric shapes, numerical analysis, and hybrid approach. Observations and field experiments after major earthquakes have shown that in hilly area building damage intensities tend to higher at hilltop than at the base. This spatial bias in building damage intensities were associated with higher levels of ground motion observation at hilltops than at the base (Çelebi, 1991). The Northridge earthquake in California (USA) resulted in peak ground acceleration (PGA) of approximate 1.78g at a small hill at Tarzana, 6 km away from the mainshock hypocentre however, at two locations at 2 km away from the hill a much lower acceleration was observed (Spudich, et al., 1996). Another classic example of ground motion being amplified due topographic feature was observed at ridge near Pacoima Dam. During the 1971 San Fernando earthquake (Mw 6.5), an accelerogram located on ridge near Pacoima Dam recorded that event highest PGA of 1.25g was even though the site was located about 8 km away from the hypocentre (Trifunac & Hudson, 1971). Studies on earthquake induce landslides have indicated that slope geometries as well as orientation influence the spatial variation in ground motions (Meunier et al., 2008; Meunier et al., 2007). Although observations have indicated that there are spatial variations of seismic motion due to topography, there are several issues that create shortfalls in this category. One of the main problem associated with observations and experiments based on instrumentation is that reference stations are limited or spatial constrained while the effects of topography may extend beyond the local topographical features (Pedersen, et al., 1994). For example 2015 Gorkha (Nepal), the Katmandu Basin received less energy as the hills surrounding the basin scattering of the seismic waves (Ashrafuzzaman & MD, 2017). In contrast, observational studies such as those based on earthquake induced landslides give a region approach on the effects of topography on seismic motion, but these are mainly qualitative as the

effects due topography is generally combined with other site factors such as geology. Furthermore, the field experiments are expensive as well as cover a small area, and may not capture activities during large earthquakes. As a means to better understand the role of topography in the modification of seismic waves as indicated by the various observations (Massa et al., 2012), numerous studies have been conducted using both analytical solutions using simple geometric shapes as well numerical simulations (Poursartip et al., 2017).

The use of analytical studies to provide a means of examining and quantifying the effects of topography in the modification of seismic waves. Studies by Trifunac (1972) and Wong & Trifunac (1974) used semi ellipsoid geometric shapes to develop analytical solutions for alluvial valleys and canyons. The classical study by Trifunac, (1972) indicated that the direction of incident SH waves influences the pattern of surface displacement. Furthermore, Wong & Trifunac (1974) study indicated that complexity in amplification of seismic motion increases with frequency of the incident plane SH-waves. Further study by Lee & Cao, (1989) indicated that amplified displacement for behind the canyon than in front of the canyon for incident SV waves. The analytical methods provide an understanding of ways in which topography modified seismic waves through simple geometric shape and orientation analysis. However, any analysis using realistic topographic geometries will make analytical methods very difficult.

To answer the shortfall in observations/field experiments after earthquakes and difficulties of analytical solution in face of realistic topographic geometries, numerical techniques have been developed. Several numerical techniques have been used to effects of the surface on seismic waves. These techniques may be classified into four groups. The first is finite differences method (FDM), which implementation is rather for simple geometries but once surface becomes complex, modelling using FDM gets problematic and difficult to implement. The second group of numerical tools, boundary element-based methods (BEM), applicable in cases where Green's function is known (Poursartip, et al., 2017). The third set of numerical tools are a finite element-based method (FEM) which implementation allows for elements of different geometry, size across an irregular grid (Moczo et al., 1997). The fourth is spectral element method (SEM) which is considered a high order variant of FEM as it includes the flexibility of FEM and the accuracy of spectral method (). Both FEM and SEM are preferred in modelling using complex and irregular surfaces as in the case where the realistic topography is used, however, SEM is easier to implement across a parallel computers (Peter et al., 2011). The fourth approach uses a hybrid approach such as parametric studies which using numerical and analytical approaches to understand the effects of topography on-site response to seismic waves (e.g. Assimaki, et al., 2005; Poursartip et al., 2017). Massa, et al., (2014) presented an overview of effects of topographic based on a hybrid of experimental observation and numerical simulation to understand site seismic response.

SEM is considered as a high order numerical method, capable of solving seismic wave equation even with a complex 3D heterogeneous model of the earth. SEM allows for accurate solution in the forward problem for generating ground motion in 3d earth model (Tromp, et al., 2008) "without increasing the number of

grid points per wavelength” (Fichtner, 2011b), a problem that limits the efficiency of FEM (Komatitsch, et al., 2013). While SEM allows for adaptation of mesh which includes an irregular surface, however, because it requires a hexahedral mesh of high quality (Komatitsch & Tromp, 1999), which may difficult to implement thus a deterrence (Casarotti et al., 2008). A high-quality mesh is needed to allow for numerical stability, acceptable geometrical distortion and number of grid points for shortest wavelength in question( Casarotti et al., 2008, Komatitsch et al., 2013). SEM is considered computationally expensive. However, the developments in computation power and the ease of implementing SEM on parallel machines have made this ever-growing method in studying effects of topography on strong ground motion (Komatitsch & Vilotte, 1998). A few examples of studies using SEM to study the effects topography on the seismic induced ground motion will be explored in the next section.

## **2.2 Effects Topography on Seismic Induced Ground Motion – SEM Applications**

SEM was first introduced in the computational fluid dynamic field by Patera (1984). As the name indicated, SEM is a hybrid of the spectral method and finite element methods. It combines the accuracy of the spectral method with the “generality” of finite element method (Patera, 1984). SEM was adapted by Komatitsch & Vilotte (1998) into the field of computational seismology to simulate wave propagation in realistic geological structures. By using a diagonal mass matrix based on Lagrange polynomial in conjunction with Gauss Lobatto Legendre quadrature to characterized the wave field within hexahedral mesh element (Komatitsch et al., 2004). Using SEM to characterise the displacement field generated by an earthquake, an integral or the weak formulation of the equation of motion is used as it best suitable for computational purposes(Komatitsch & Tromp, 1999; Fichtner, 2011). It is this weak formulation, which allows for the inclusion of realistic topography and accurate simulation of surface waves (Komatitsch & Tromp, 1999). Komatitsch et al. (1998) illustrated the effects of topography using a 2D geological structure in the Andes first with a homogeneous velocity and density model followed by using an estimated velocity model. In both cases, SEM was able to show that topography resulted in diffracted seismic signals. The study also indicated that amplification occurs near the summit of a modelled Gaussian shape hill as well as a directivity effect due to topography.

Magnoni et al. (2014) used SEM to simulate seismic waveforms in the presence of topography and complex geology which were compared with observed data. They used a finite source model to represent the 2009 Mw 6.3 L’Aquila earthquake and 3D model that covers a region of 200km x 200km x 60km in central Italy. By using the SEM software package SPECFEM 3D Cartesian, they were able to accurately simulate ground motion as well as indicated that topography produced scattering and amplification of seismic waves. The study also indicated that for near source regions for moderate to large earthquakes, the simulation produced waveforms that were very comparable to observed signals.

The 1999 Mw 7.6 Chi-Chi earthquake in Taiwan had resulted in significant damages for a number of superstructures (Lew, et al., 2000). In light of this, several studies were conducted using SEM to investigate

the effect that topography has on the seismic motion within Taiwan (Lee, et al., 2014; Lee, et al., 2009a; Lee, et al., 2009b; Lee, et al., 2008). In a study by Lee et al. (2008) a very detailed topographic model was used for entire Taiwan, at a resolution of 40m. This simulation had required 116 gigabytes of memory and a simulation time of 9.5hrs. Although this simulation indicated how computation expensive SEM may be, none the less, the inclusion of very detailed topography had allowed for greater analysis of effects of topography on the seismic motion. This study also included detail meshing of the Taipei basin and as such was able to provide an insight into effects of both surface topography and basin effects. Lee et al., (2009b) used a 40m topography model and studied the effects of topography for large earthquake scenarios by using a double-couple point source, a bilateral rupture, an eastward rupture and a westward rupture. The study had indicated that source rupture process varies the effects of topography on ground motion. Lee et al., (2009a) used a very detailed topography model based on 1 m light detection and ranging (LiDAR) digital terrain model (DTM) for the Shamao Mountain. The LiDAR DTM showed very detailed features of the ridges and valleys that were not observed in the 40 m digital elevation model (DEM) mesh of the same area. Using SEM to simulate a hypothetical earthquake based on double couple point source model, the LiDAR-based model indicated stronger ground acceleration patterns.

A study by Khan et al., (2017) indicated that modelling the effects of topography using a mesh and DEM resolution of 540m or greater produces unrealistic results when compared with models of the highest resolution available. In contrast, models based on 270m or finer produces a more similar result to the highest resolution models.

Ashrafuzzaman (2017) had used SEM to model the effects of surface topography on a seismic ground motion for the 2015 Mw 7.8 Gorkha earthquake and relate the surface amplification to building damages. The building damage inventories for this area had many inconsistencies which limited the effectiveness of the correlation.

The reviewed examples have shown that SEM is useful for simulation earthquake as well as quantifying the effects of topography on the seismic motion. However, the resolution of the topography model will influence the effects of topography. The tradeoff between resolution and computation cost will depend on the scale of analysis as well as the computation power available. The way in which the quantified effects relate to site response in case landslide or building damages is no studied by most of these examples except the studied by Ashrafuzzaman (2017). In an area where both landslide and building damage inventories are available, SEM may allow for a greater understanding of effects of topography on the seismic ground motion as related to site response as in the case in Haiti. Such an analysis is yet to be covered.

## 3 2010 M<sub>w</sub> 7.0 HAITI EARTHQUAKE: REVIEW

This chapter provides a review of the tectonic setting and seismicity in Haiti to have a better understanding of the occurrence of the 2010 Mw 7.0 Haiti earthquake. A general overview of the studies explored to understand the associated site response due to the earthquake as well as the earthquake-induced building damage assessment that was undertaken by three international agencies. Finally, the research gap that needed to be filled is also identified and based which this study is carried out

### 3.1 Seismo-tectonic setting of Hispaniola

Haiti is located on the tropical island of Hispaniola which is situated within the plate boundary zone between North American plate and the Caribbean plate (Douilly et al., 2013). The relative motion of the Caribbean plate to the North American plate is moving at an oblique angle with relative motion of 20 mm/ y (DeMets et al., 2000). In fact, the current structural geology of Hispaniola (Figure3.1a) is an indication of the oblique motion of the Caribbean plate with respect to the North American plate resulting series of thrust folds and belts (Mann et al., 1991; Manaker et al., 2008). In Haiti, the relative oblique motion of the Caribbean plate and associated deformation are transferred to the two-major strike-slip faults, the Enriquillo Plantain Garden Fault Zone (EPGFZ) in the south and the Septentrional- Oriental Fault Zone (SOFZ) in the North as well as series of thrust fault (Mann et al., 1995). Bounded between these strike-slip faults are a series of folds and ramp basins as result of thrusting which is exemplified by Trans-Haitian fold and thrust belt and Cul de Sac- Enriquillo ramp basin respectively (Figure3.1b).

The EPGFZ and SOFZ have several major ruptures in the past. Ali et al. (2008) indicated EPGF had major events in 1770, 1751 and SOF in 1887 and 1842 (Figure3.1a). The build-up of seismic stress is usually released by an earthquake in the upper crust. Both strike-slip fault systems work together as one, where an event on one fault tends to release stress in both as similar and consistent regional stress field produces varied geomechanical response due to geological heterogeneity (Mann et al., 1995). Ali et al. (2008) alluded that the last major rupture on both systems then a return period of 250yrs for major events. Being that these two strike-slip faults systems are the main stress accommodators; they are normally considered as the source of major seismic hazards. Therefore, this leads many to initially attribute the 2010 earthquake (M 7.0) to the EPGFZ. However, a study by Nettles & Hjörleifsdóttir (2010) highlighted that most of the aftershocks showed reverse slip (thrusting) which is unexpected for an earthquake on a strike-slip fault. Further studies by Calais et al. (2010), and Mercier de Lépinay et al. (2011) have suggested that this earthquake should be attributed to the Leogane fault, which was previously unmapped (Figure3.2 a & b). Subsequently, a study by St Fleur et al. (2015) indicated that earthquake involved a combination of the Lamentin thrust and the EPGFZ which helps characterize the reverse-slip and strike-slip components of the event (Figure 3.2 a & c). These studies have provided an insight into the complex and poorly understand seismo-tectonic setting in Haiti as result of the earthquake. Furthermore, both solutions have indicated that initiated on a thrust

fault with some contribution from the EPGFZ. Hence the EPGFZ remains of great concern and there is a need for further studies not only to characterised the earthquake but also the interaction of the seismic wave with the surface..

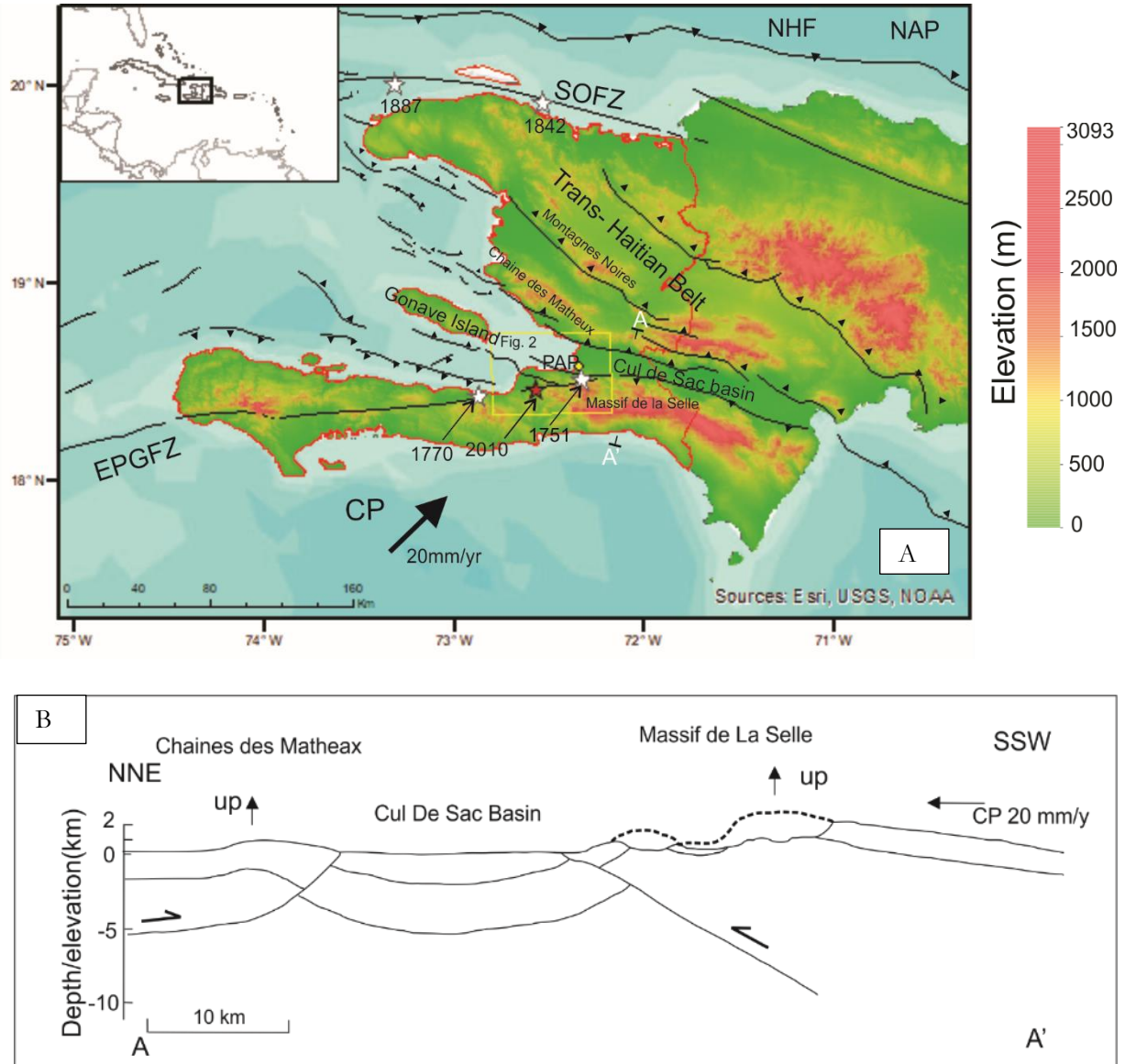


Figure 3.1: Seismo-tectonic setting of Hispaniola [a] tectonic setting of Hispaniola ( modified from Corbeau et al., 2017, p. 10) . SOFZ is the Septentrional- Oriental Fault Zone, EPGFZ is the Enriquillo Plantain Garden Fault Zone, H=NHF is the North Hispaniola Fault, CP is the Caribbean Plate, NAP is the North American Plate. The red star is 2010 Mw 7.0 earthquake and white stars are historical earthquake. The large arrow indicate the relative motion of the Caribbean plate to the North American Plate at 20 mm/y (DeMets et al., 2000), essentially pushing Hispaniola into a smaller space resulting several thrust faults producing basin and fold mountains.[b] The cross section is shows how the region is being modified by thrust faults due to continued relative motion of the Caribbean plate towards the North American plate building up stress along the faults.

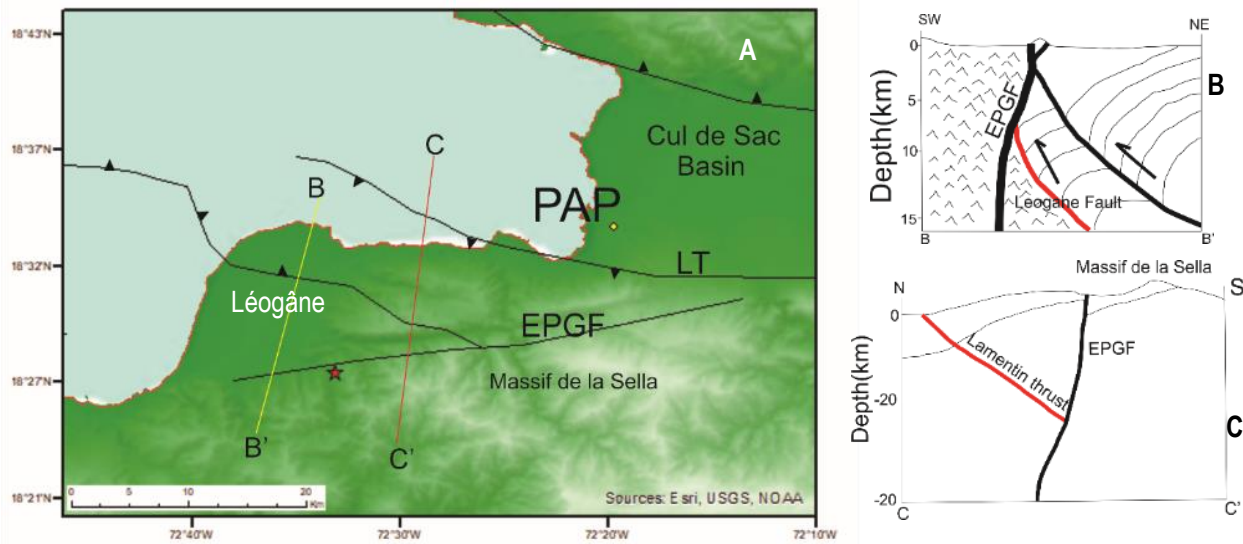


Figure 3.2: The fault mechanism for the Mw 7.0 earthquake 2010 with profiles B-B' and C-C'. PAP – Port au Prince, LT – Lamentin Thrust, and EPGF -Enriquillo Plantain Garden Fault. B-B' profile shows the fault orientation attribute to generate the earthquake by (Calais et al. 2010). C-C' profile shows the fault orientation attribute to generate the earthquake (St Fleur et al. 2015). Each profile does not consider the other fault orientation.

### 3.2 Earthquake-induced ground motion: Site response

The site response to an earthquake may be expressed based on damages to superficial structures such as building or deformation and mass movement relating to the ground. An examination of the earthquake-induced building damage assessment will follow in the next section. To have better understating of this site response numerous studies were conducted.

In the absence of strong motion data, Hough et al. (2012) used macroseismic induced movement to estimate peak ground acceleration (PGA) around 0.2g in most of the areas in Port-au-Prince, with some areas experiencing higher ground motion due to local amplification. They examined the markings left on the floor by an industrial battery rack at Canape Vert and used the empirical relationship established by Taniguchi & Miwa (2007) to estimate slip displacement for the industrial rack which had experienced sinusoidal ground acceleration due to the earthquake. The peak horizontal ground acceleration is equivalent to the amplitude of the horizontal sinusoidal ground acceleration for a rigid body on the ground floor (Taniguchi & Miwa, 2007).

Douilly et al. (2016) showed that a low seismic velocity zone below Léogâne basin, Haiti. The city of Léogâne suffered significant damage, with approximate 80% to 90% of the buildings destroyed (DesRoches et al., 2011). The study by Douilly et al. (2016) used tomographic inversion imaging to characterised velocity structure in southern Haiti. Low-velocity zones have been indicated to result in amplified ground motion as shown by Komatitsch et al. (2004) for the Los Angeles basin. Therefore, Léogâne might have experienced amplification due to unconsolidated sediment lithology. The city of Port-au-Prince also experienced

significant damage however, it is located at the southern edge of the Cul-de-Sac plain, on the foot hill of Massif de la Sella (St Fleur et al. 2016). Being that the city is situated at the foot hills, it sits on top of successive episodes of sediments that created a complex topography and melange superficial geology as such sediments induced amplification might play a moderate role on the ground motion for the 2010 earthquake event (St Fleur et al., 2016).

The boundary region of the Cul-de-Sac basin is marked by a series of hills, and associated valleys, which might introduce topographic amplification. Rathje et al. (2011) indicated that several damaged buildings in the Cul-de-Sac basin, especially at its edge, could have experienced topographic amplification. Particularly those areas that have higher slope gradients than the surrounding basin (figure 2). Furthermore, both Rathje et al. (2011) and Assimaki & Jeong (2013) have indicated that topographic amplification, as well as geological conditions, may have contributed to damages to Hotel Montana.

Gorum et al. (2013) studied the distribution of earthquake-induced landslides in Haiti and indicated qualitatively that topography difference along with tectonic setting explains the distribution. However, the extent to which topographic induced amplification could explain the distribution remains a question to be answered.

### **3.3 Earthquake-induced - Building Damage Assessment**

Numerous buildings in several towns and the capital Port-au-Prince, Haiti were damaged or destroyed due to the 2010 7.0 Mw earthquake as such several studies were conducted to estimate the damage levels and the buildings damaged.

A study by DesRoches et al. (2011) provided an account of the damage as result of the 2010 Haiti earthquake. Although the study gave an idea of the distribution of the building types based on the inventory compiled by Haitian Ministry of Statistics and Informatics (IHSI) across the Haiti, it did not provide damage distribution across the building types.

Marshall et al., (2011) and Paultre et al., (2013) indicated many of residential buildings were based on the infill masonry construction type and used poor quality materials. The studies indicated that most of these buildings suffered significant damages during the earthquake. Paultre et al., (2013) also indicated that many of the engineered structures did not consider earthquake loading. As such both engineered and non-engineered structures both suffer significant damages. In fact, Paultre et al. indicated that the damage sustained to Hotel Montana could be a combination of poor engineering and site induced seismic amplification. The columns cross sections were too small, with little 'longitudinal reinforcement, and almost no transverse reinforcement' (Paultre et al., 2013, p. 10).

EC-JRC et al., (2010) conducted a building damage assessment across several towns and Port-au-Prince. They assigned five grades for different damage levels (D1: negligible to slight damage, D2: moderate damage, D3: substantial to heavy damage, D4: very heavy damage, and D5: destruction), which were based on the European Macroseismic Scale (EMS 98) 1998 (Grünthal, 1998). The assessment used remote sensed data along with field observation to validate the assessment. A brief description of the various remote sensed data used for building damage assessment is presented in the next section.

### Optical Remote Sensing Damage Assessment

Optical remote sensed data were used to characterise the earthquake-induced damage with a primary focus on buildings. Corbane et al. (2011) indicated that joint building damage assessments were conducted under the auspices of three international agencies. These are World Bank WB, the United Nations Institute for Training and Research (UNITAR) Operational Satellite Application Programme (UNOSAT) and the European Commission's Joint Research Centre (JRC) using both high-resolution satellite and aerial imagery (figure 3). The building damage inventories generated through UNOSAT and JRC were by remote sensing specialists using manual photo-interpretation. The World Bank along with ImageCat and Earthquake Engineering Research Institute (EERI) formed the Global Earth Observation – Catastrophe Network (GEO-CAN) community. GEO-CAN used the global geoscience and engineering community to aid in the damage assessment. As indicated before, the joint assessments based their damage grade on EMS 98. However, Kerle (2013) expressed reservation in using EMS 98 scale for image-based assessment as it is designed for on the ground damage assessment by structural engineers. Furthermore, these image-based assessments were near nadir and did not correctly categorised some buildings which had pancaked or undergone soft story collapse (Gerke & Kerle, 2011). Gerke & Kerle (2011) suggested the use of off-nadir airborne imagery such as Pictometry to obtain a better understanding of building damage grade. However, Booth et al. (2011) indicated that although Pictometry data is promising and ground observation is ideal for doing the building damage assessment, the extensiveness of the damaged buildings in Haiti made the use satellite and aerial imagery very effective.

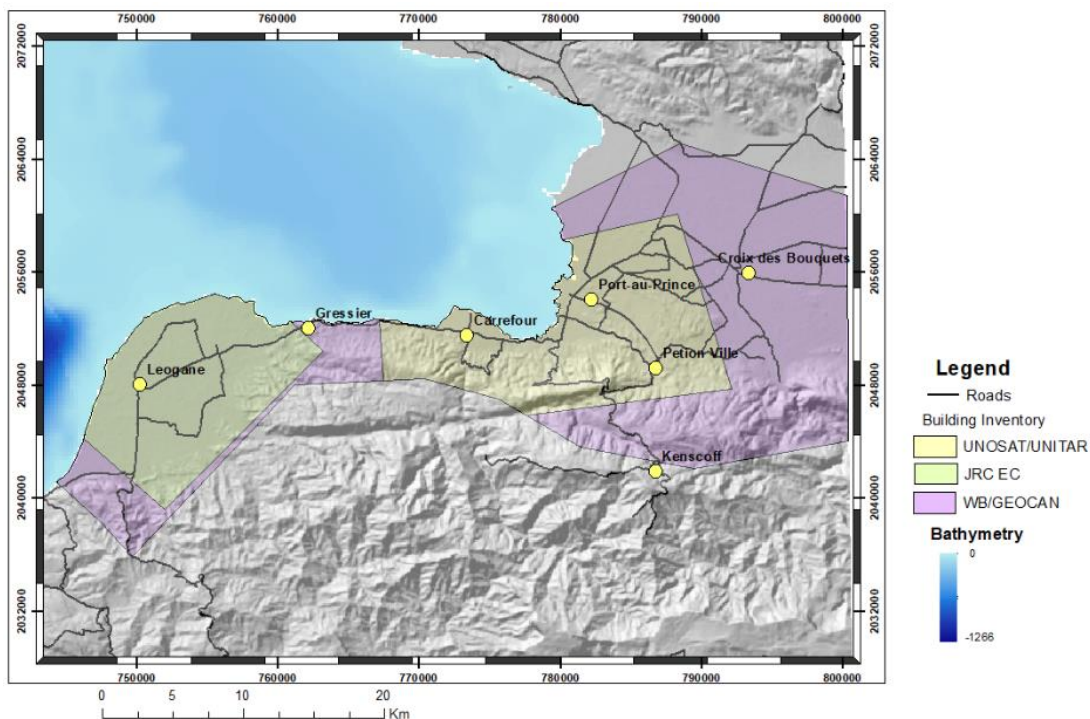


Figure 3.3 showing the damage assessment extent from Léogâne to Cul-De-Sac basin.

### **Active Remote Sensing Damage assessment**

Both LiDAR and Synthetic Aperture Radar (SAR) data were collected after the earthquake in Haiti and used to characterise building damages. Upreti & Yamazaki (2012) had applied SAR data from TerraSAR -X to characterise damaged buildings in Port au Prince. The study indicated the usefulness of SAR for building damage assessment since radar remote sensing is not affected by clouds. However, the complex building structures in communities around Port au Prince makes using SAR data very complicated especially when examining the damaged buildings. Ural et al. (2011) used a combination of LiDAR and very high-resolution satellite image to damage pattern in Port au Prince. However, categorising buildings damage level may be difficult, especially for those that experienced pancaking due to lack of pre-event LiDAR. The integration of LiDAR and optical remote sensing have been illustrated to be an aid in damage assessment, the lack of pre-event LiDAR data limits usefulness in damage assessment.

As indicated in the above review, several pieces of research have tried to understand the 2010 Mw 7.0 earthquake. Similarly, numerous studies have been done on the building damage inventories. However, few studies have attempted to explore the building damages as they relate with topographic amplification. Furthermore, these studies have examined the relationship in a qualitative or at a local scale. Quantitatively research looking at a large scale at the effects of topography and the associated site response is the next step following these studies; however, no research has yet explored this phenomenon.

## 4 METHODOLOGY

The methodology comprises of two stages: the simulation of the earthquake and the comparison of the simulated results with observed landslides and building damage inventories. The Spectral Element Method (SEM) was used for the simulation of the earthquake and principles behind the method is presented where necessary. In this chapter, the two stages are expounded on by indicating the purpose, the software and datasets used as well as research steps taken to achieve various findings.

### 4.1 First stage: Simulation of the earthquake

#### 4.1.1 Purpose

The purpose of this stage is to simulate the 2010 Mw 7.0 Haiti earthquake within a 3D model of a section of the earth.

#### 4.1.2 Dataset

Two sets of data were used for the first stage: namely surface data and earthquake source data.

The surface data comprises of bathymetry and topographical data. Bathymetry was obtained from General Bathymetric Chart of the Oceans at a resolution of 30 arc-second, and Shuttle Radar Topography Mission (SRTM) datasets at 90m were used to generate the surface topography. Although both Advance Spaceborne Thermal Emission Radiometer – Global Digital Elevation Model (ASTER GDEM) and SRTM DEMs are freely available, Shafique et al. (2011) and Suwandana et al. (2012) indicated SRTM DEMs are better at estimate vertical height and terrain characteristic than ASTER GDEMs. Additionally, the study area is located in the tropics and the possibility that there is for cloud removal from the ASTER DEM makes it less suitable than the SRTM DEM.

Centroid Moment Tensor (CMT) obtained from [www.globalcmt.org](http://www.globalcmt.org) and was used as the seismic source.

Seismogram obtained for the 2010 Mw 7.0 Haiti earthquake was accessed from Incorporated Research Institution for Seismology (IRIS) Wilber 3 event page at [www.ds.iris.edu/wilber3/find\\_stations/2843110](http://www.ds.iris.edu/wilber3/find_stations/2843110).

#### 4.1.3 Software

CUBIT 13.0 was used to generate the finite element mesh used in the simulation. This software is used to create finite element mesh (Blacker et al., 2016) and recommended by Casarotti et al., (2008) for mesh generation for earthquake simulation using SPECFEM 3D (CIG, 2015). The GEOCUBIT script was used with CUBIT to generate a semi-automated process for mesh creation (Casarotti et al., 2008).

SPECFEM3D Cartesian is an open source code developed using the principles of SEM. The software developed by Computational Infrastructure for Geodynamics to simulate seismic event and associated ground motion (CIG, 2015).

MATLAB was used to plot the synthetic seismograms obtained from the seismic simulation and observed seismograms from the nearest seismic station to the study area. MATLAB was also used to remove the lag between the synthetic seismogram and the observed seismograms to allow for comparisons.

Finally, ArcGIS was used to combine bathymetry and topographic data need to generate a surface model that would be incorporated with the mesh for the study area. The generated ground motion data obtained SPECSEM3D was in the format of cartesian format and was plotted using ArcGIS to create ground motion maps and the amplification maps.

#### 4.1.4 Methodology

The simulation of seismic event can be accomplished in six steps:

1- A continuous surface topography was created that includes the CMT location and the areas where site response will be investigated. ArcGIS was used to integrate bathymetry data with SRTM data into a continuous surface or Digital Elevation Model (DEM) at 90m. Although Khan et al. (2017) indicated for effective and efficient simulation of a seismic event in areas with irregular topography, a DEM of 270m could be used. The study shows that at higher resolutions SEM becomes very computational expensive although there are improvements in accuracy and at a lower resolution it will result in inaccuracy. However, a mesh 90m was used in this study because it captured the terrain.

2- The creation of a finite element mesh is considered the most critical stage for accurate simulation of seismic waves (Casarotti et al., 2008; Komatitsch et al., 2013). GEOCUBIT script was used along with CUBIT to generate a hexahedral mesh with realistic topography for parts of the Port Au Prince bay, parts of Cul-de-Sac basin, and surrounding hills. The process was repeated for the same area but without topography. SEM requires that hexahedral elements be used in the mesh, which results in skewed elements. Skewness is the measurement of distortion as the element, and as the element becomes very distorted, the numerical errors will occur. The creation of mesh for seismic simulation requires elements of skewness ( $s$ )  $< 0.8$  (Casarotti et al., 2008), which is sometimes difficult for a hexahedral based mesh. A mesh resolution of 180m was used to characterised the surface topography although Khan et al. (2017) indicated that 270m mesh was effective resolution to capture surface topography for seismic analysis. However, a mesh resolution was effective at capturing the surface topography. Based on the resolution of the mesh, the model was defined as 180m resolution.

3-The mesh generated by using CUBIT was exported into the SPECSEM3D Cartesian format. The earthquake source used in the simulation for the Mw 7 Haiti earthquake was the Centroid Moment Tensor (CMT). Moment tensor is a representation of the forces associated with a fault, where one set of forces indicate the direction of slip (Madariaga, 2007). The CMT representation of an earthquake is viewed as a point source as it provides the six moment-tensors, location and time of the event (Ekström et al., 2012). The CMT acts as the seismic source, as SPECSEM3D tries to solve the seismic equation:

$$\rho \partial_t^2 s = \nabla \cdot T + f \quad 4.1$$

where  $s$  is the displacement wavefield ( $x, t$ ),  $\rho$  is the mass density,  $T$  is the stress tensor, and  $f$  is the seismic source. The stress tensor  $T$  is linearly related to the strain (Peter et al., 2011):

$$T = c: \nabla s, \quad 4.2$$

where  $c$  denotes the stiffness tensor characterized the medium elastic properties.

With a meshed model and the seismic source characterised, the basis function to represent the unknown displacement vector and test vector on each element is to be defined (Komatitsch et al., 2013). As such points ( $x, y, z$ ) within each hexahedral element is related to points in a reference cube (figure 4.1). This mapping is expressed by a function

$$x(\xi) = \sum_{A=1}^M \mathbf{X}_A \mathbf{N}_A(\xi) \quad 4.3$$

The  $A=1, \dots, M$  anchors  $\mathbf{X}_A = \mathbf{X}(\xi_A, \eta_A, \zeta_A)$  and  $\mathbf{N}_A(\xi)$  which is the shape function defines the geometry of the element. A 4 – 10 degree Lagrange polynomials is used in defining the hexahedral shape functions  $\mathbf{N}_A(\xi)$  used in SEM (Dimitri Komatitsch et al., 2013).

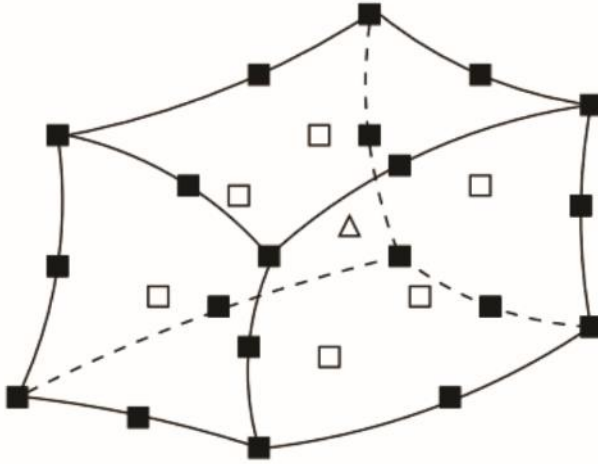


Figure 4.1: The geometry of hexagonal finite element. The anchor points defined the defined the geometry of the element such that the edges, corner, faces of the element are defined by the a node (Tromp, et al., 2008, p. 8). The mapping of element to reference cube is done by a combination of high Lagrange polynomial with Gauss Lobatto Legendre (GLL) points see figure 4.2

The  $n+1$  Lagrange polynomial of  $n$  degree are defined in terms of  $n+1$  control points  $-1 \leq \xi_\alpha \leq 1, \alpha=0, \dots, n$ , by

$$h_\alpha(\xi) = \frac{(\xi - \xi_0) \dots (\xi - \xi_{\alpha-1})(\xi - \xi_{\alpha+1}) \dots (\xi - \xi_n)}{(\xi_\alpha - \xi_0) \dots (\xi_\alpha - \xi_{\alpha-1})(\xi_\alpha - \xi_{\alpha+1}) \dots (\xi_\alpha - \xi_n)}$$

In a 3D environment, the Gauss Lobatto Legendre (GLL) points of  $(n+1)^3$  are the controlled points  $\xi_\alpha, \alpha=0, \dots, n$ , needed to define the Lagrange polynomials of degree  $n$ . Figure 2 illustrates the characteristic of a Lagrange polynomial of 4 degrees. This combination of the GLL points and Lagrange polynomial using a diagonal mass matrix in SEM leads to a more accurate numerical approach than other methods such as finite elements. Using a polynomials degree of 4 or 5 provides a balance between accuracy and time-integration stability (Fichtner, 2011a).

A polynomials degree of 4 was used which means that 125 Gauss Lobatto Legendre GLL points contained in each element. The polynomial order  $N$  and the element size ( $d$ ) are restricted by the shortest wavelength

( $\lambda_{Min}$ ) that pass through the model (Cupillard et al., 2012). Komatitsch & Vilotte (1998) indicated that at least five GLL nodes per minimal wavelength to ensure accuracy and relationship between element size and wavelength is characterized by:

$$d \leq \frac{N}{5} \lambda_{Min}. \quad 4.4$$

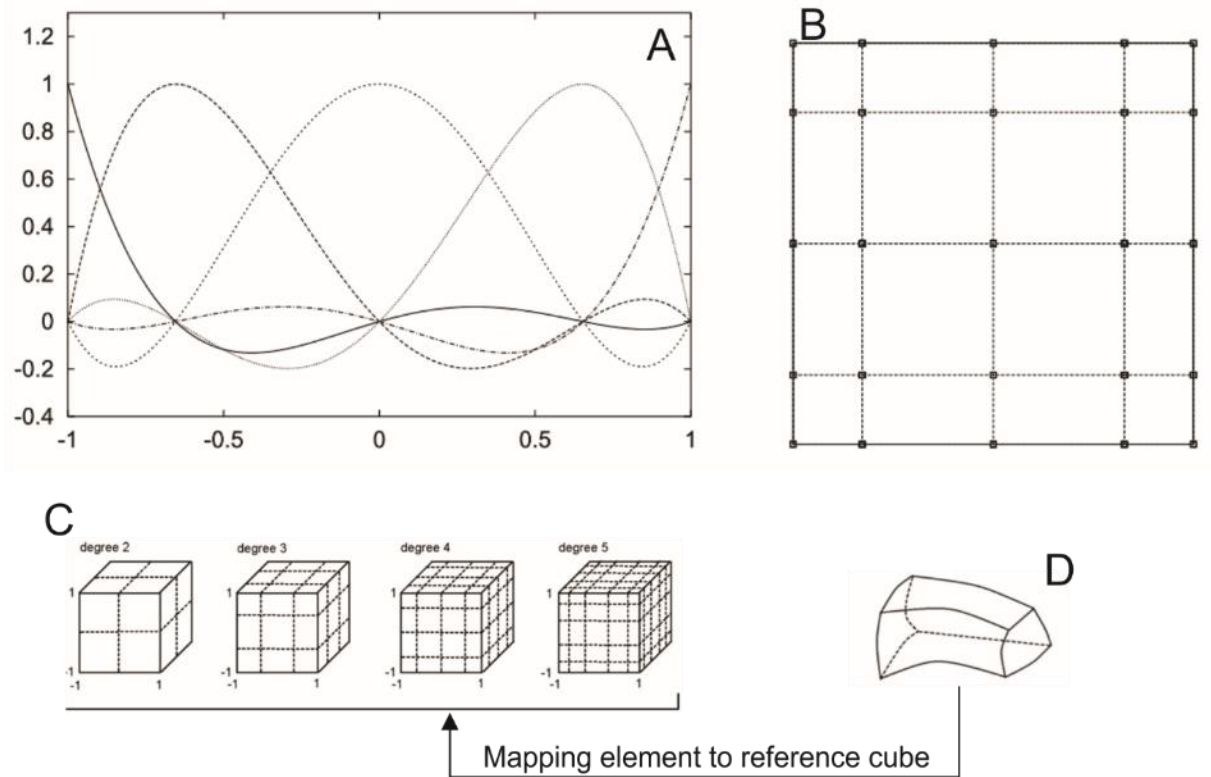


Figure 4.2: Mapping to reference section [-1,1], where  $N+1$  GLL points are for Lagrange of 4 degree showing by 2 A and 2B. 2C represents reference cube characterized by  $(N+1)^3$  GLL points (indicated by the intersection of the dash lines as well as solid lines) for different polynomial degree for mapping element at 2D (modified from Tromp et al., 2008, p. 9; Fichtner, 2011, p72)

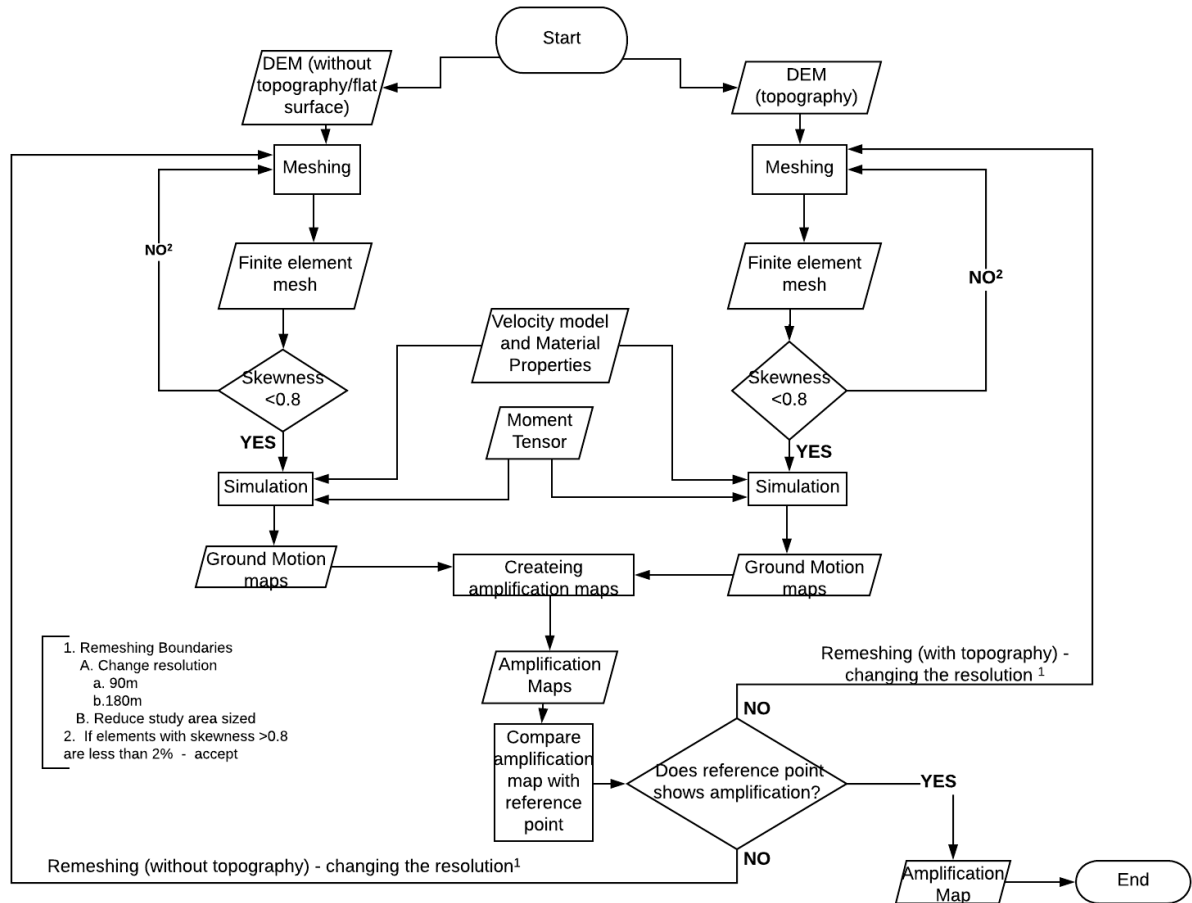


Figure 4.3: Showing the methodological flowchart for ground motion modelling

The material properties (velocity of P wave ( $V_p$ ) and S wave ( $V_s$ ); density of the material and attenuation) for the element were defined before the simulation commenced. No attenuation was used in the model for the bedrock. The velocity for P wave was set at 6600 m/s and S wave was set at 3600m/s, with a ratio of  $V_p/V_s$  of 1.83 and density of 3500kg/m<sup>3</sup>. The velocity model was obtained from (Douilly et al., 2013). An empirical relationship of density to the velocity of the primary wave ( $V_p$ ) developed by Stidham (as cited by Lee et al., 2008 p. 255),  $\rho = V_p/3+1280$ . The density 3500kg/m<sup>3</sup> was used as the  $\rho$  value was expressed in the nearest hundredth. As no seismic research stations located in Haiti, several test seismographs were placed across the model to evaluate the seismic wave propagation across the model (Ishii et al., 2005; Fletcher et al., 2006). The synthetic seismograms were compared with the seismic data from Presa de Sabaneta, Dominican Republic, the closest seismic station to the study area.

Once the material properties have been defined, the length of time step was defined based on the following condition:

$$\Delta t < C \min \Omega (h/v) \quad 4.5$$

where C is denoting the Courant number and the  $\Omega$  is the model volume,  $h/v$  ratio between grid space and velocity P ( $V_p$ ) (CIG, 2015; Komatitsch et al., 2013). The grid space is related element size and number of GLL points. Furthermore, the length of simulation used was 50 seconds (length of simulation is defined as

the number of time steps and length of each time step). The simulation was performed using mesh with topography as well as mesh without topography (perfectly flat) for the study area (figure 4.3). The results from the simulation were used to generate ground motion map for the study area.

4- Ground motions were characterized by Peak Ground Displacement (PGD). PGD data were used to create ground motion map in terms of absolute values, which was used for further analysis as SEM technique better suited for low-frequency ground displacement (Dhanya et al., 2017). The ground motion data (PGD) and synthetic seismogram obtained after simulation were generated in ASCII format which were plotted using ArcGIS and MATLAB respectively. The synthetic seismograms were stacked in MATLAB to have an idea if the model source location is indicated by the seismograms. The farthest seismogram from the source was compared with the seismic data from Presa de Sabaneta, Dominican Republic, which is the nearest observed seismogram to determine correlation using MATLAB.

5-Amplification model was created by using both the ground motion maps with and without topography as indicated by the following formula:

$$GAF = \frac{Gm_A - Gm_B}{Gm_B} \times 100 \quad (\text{modified from Lee et al., 2008}) \quad 4.6$$

Where GAR = Ground Motion Amplification Factor,  $Gm_A$  is ground motion model with Topography and  $Gm_B$  is ground motion model without topography. The PGD maps were used to create the amplification model.

6- As there is no seismic research station in Haiti at the time of the earthquake, the amplification model was compared with known area that experienced topographic amplification, Hotel Montana as well as landslide data to test model. After, the comparison, the model was used in the next stage, where they were compared with damaged building inventories for the study area.

## 4.2 Second stage: Comparison of simulation and observations

Comparison Model Results with earthquake-induced landslide data and earthquake-induced building damage inventories. This section was separated into two parts. Part A looked at the relationship with landslide data and the amplified ground motion as well as PGD. Part B examined the relationship between amplified ground motion and building damages in Cul-de-Sac Basin.

### 4.2.1 Dataset

Three sets of data were used for the second stage:

The landslide datasets used were based on landslide inventories by Gorum et al. (2013) which are hosted by USGS at [www.sciencebase.gov/catalog](http://www.sciencebase.gov/catalog). The landslides were mapped using GeoEye 2 and WorldView 2 with spatial resolution of 0.6 to 1m based on monoscope image interpretation of pre and post-earthquake scenes. The landslides were mapped as polygons with a minimum threshold of 14.1m<sup>2</sup> and approximately

95% of the landslides triggered by the earthquake mapped. The landslides were projected using the Universal Transverse Mercator Zone 18 North based on World Geodetic System 1984 (UTM 18N WGS 1984). The building damage inventories used in the analysis were based on the GEOCAN and UNOSAT inventories which were part of the integrated dataset of “Remote sensing damage assessment: UNITAR/UNOSAT, EC JRC and World Bank.” This dataset was obtained from United Nation Institute for Training and Research (UNITAR) at [www.unitar.org/unosat/haiti-earthquake-2010-remote-sensing-based-building-damage-assessment-data](http://www.unitar.org/unosat/haiti-earthquake-2010-remote-sensing-based-building-damage-assessment-data). The buildings were using very high-resolution imagery (World View 2 at 0.5m, QuickBird -2 at 0.6m and aerial photos at 0.15m). The was projected using UTM 18N based on the North American Datum 1983 (NAD 83). The dataset was presented as point features. Lemoine et al. (2013) conducted a validation study for the combined building assessment against ground survey with an overall accuracy of 73% and against Pictometry of 1247 building in Port au Prince with an overall accuracy of 79%. However, the combined building assessment for building classified as damage grade 5 had commission error of 68 and damage grade 4 had omission error of 80 based on the Pictometry survey.

Part A: The methodology for analysis of modelled results and landslide data were conducted in three steps. 1-The landslide data were obtained as polygon data but were converted to point data (figure 4.4). Point data were used for the analysis as not all the landslides had a defined body and scarp regions. The point that represented the maximum elevation of each landslide were assigned the attributes from the inventory.

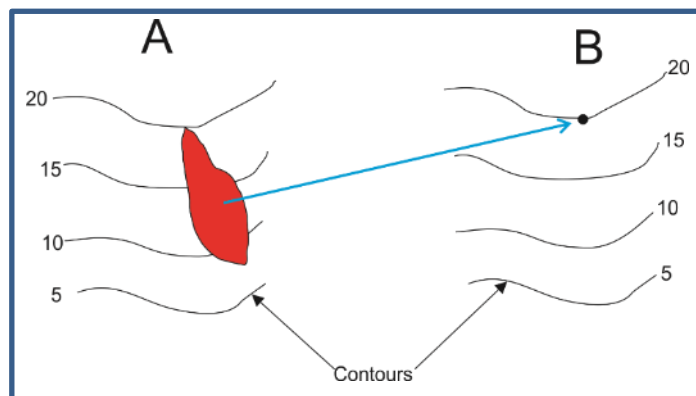


Figure 4.4: Landslide represented as polygon in A as in landslide inventory from Gorum et al. (2013) and B is representation of a landslide being represented as point data as in B. The landslide attribute has been mapped to the point data as indicate by the blue arrow and the point is located at the maximum elevation of the landslide.

2- The landslide point data were spatially overlaid on the ground amplification maps model and amplification value extracted for each landslide. The landslides with their associated amplification was classified into eight categories (Table 4.1) to simplified the distribution and to get summary of the distribution. The PGD amplification map was classified based on the modified Gorum et al., 2011 landslide density class for earthquake induced landslides. Then statistical analysis was conducted to the relationship between amplification values and landslide orientations and position. The landslide orientation and positions examined were the distance from the seismic source, back azimuth from the seismic source, slope orientation based on the studies by Meunier et al. (2007) and Meunier et al. (2008). The mean of the box

plot was to indicate the dominant slope orientation for the landslide with respect to amplification. For the back azimuth a rose diagram was used to extrapolate the dominant azimuth. A scatterplot analysis was conducted for azimuth against PGA amplification to determine if there is relationship with azimuth an amplification of landslide

3- Landslide density map for the landslide data was generated using the method used by Gorum et al. (2011) to compute landslide density. A kernel of 1km was used to compute the percentage of landslides in that area and represented at a pixel size of 180m based on the resolution of the amplification map. The landslide density map was spatially overlaid with the amplification maps. Then the spatial pattern of the landslides was analysed with respect to classified amplification.

Table 4.1: PGD Amplification Classification

	<b>Amplification Classification</b>	<b>PGD Amplification</b>
<b>Amplification / Deamplification</b>	High Amplification	>40
	Moderate Amplification	40> amp >10
	Low Amplification	10>amp >0
	Low Deamplification	0 < amp >-10
	Moderate Deamplification	-10 < amp > -40
	High Deamplification	<-40

Part B: The methodology for analysis of ground motion results and building inventories were accomplished in two steps.

1- The building inventories of GEO-CAN and UNOSAT were considered for this study as they cover a large part of the Cul de Sac basin, unlike the EC-JRC inventory which covers mainly the Léogâne area (figure 4.5). Both GEO-CAN and UNOSAT used the remote sensing building inventory assessment based on the EMS -98 (Grünthal, 1998) which comprises of five categories as a basis for the classification (figure 4.6). The dataset was comprised of four categories (Table 4.2) and was examined for similarities and dissimilarities to determine how the inventories were to be used. The GEO-CAN dataset was more extensively distributed across the Cul de Sac but comprised of two damage grades (GRADE 4 and 5). The GEO-CAN inventory was based on the used on post- earthquake aerial photographs to map damaged buildings in Haiti in combination with pre-earthquake satellite imagery. The mapping was conducted by volunteers from the earthquake engineering and earth science communities using grid based approach to map very heavy damaged and destroyed buildings (EMS Grade 4 and 5) (Rathje et al., 2011). The UNOSAT dataset was mostly around the Port-au-Prince area but had four damage grades. The UNOSAT inventory was conducted by remote sensing specialists to map damaged building based on EMS scale into four damage classes: no visible damage; substantial to heavy damage; very heavy damage and destruction as shown in Table 4.2. An accuracy assessment based on field observation indicated that both inventories has an accuracy approximate 77%.

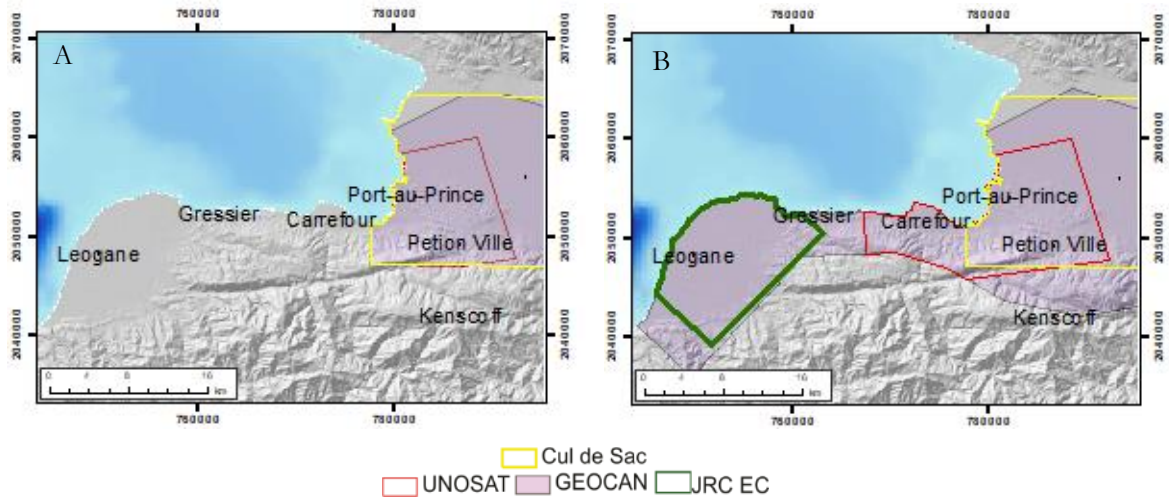


Figure 4.5: Distribution of Building Inventory (A) the extent of the damage inventories that were explored in the study; (B) shows the extent of the damage inventories in the study area

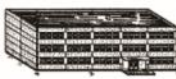
Masonry Buildings	Reinforced concrete Buildings	Classification of damages
		Grade 1: Negligible to slight damage (no structural damage, slight non-structural damage) Fine cracks in plaster over frame members or in walls at the base. Fine cracks in partitions and infills.
		Grade 2: Moderate damage (slight structural damage, moderate non-structural damage) Cracks in columns and beams of frames and in structural walls Cracks in many walls
		Grade 3: Substantial to heavy damage (moderate structural damage, heavy non-structural damage) Large and extensive cracks in most walls. Roof tiles detach Cracks in columns and beam column joints of frames at the base and at joints of coupled walls.
		Grade 4: Very heavy damage (heavy structural damage, very heavy non-structural damage) Collapse of a few columns or of a single upper floor Serious failure of walls; partial structural failure of roofs and floors.
		Grade 5: Destruction (very heavy structural damage) Total or near total collapse.

Figure 4.6: European Macroseismic scale 1998 (EMS 98) (modified from Grünthal, 1998)

Table 4.2: Damage Grade for the Building Inventory

Damage Grade	Explanation used by Inventories
EMS Grade 1 (negligible damage) or EMS Grade 2 (moderate damage) or Grade 0 (no damage)	No Visible Damage
EMS Grade 3	Substantial damage to Heavy Damage
Grade 4	Very Heavy Damage
Grade 5 (total or near total collapse)	Destruction

2- The UNOSAT inventory was used for analysis with the PGD amplification maps as it had mapped buildings at four different classes. However, the no visible damage and the substantial to heavy damage were combined into no to moderate damage class. Rathje & Adams (2008) indicated that EMS Grade 3 was difficult to be categorised by remote sensed satellite data. The damage classes of very heavy damage (EMS Grade 4) and destruction (EMS Grade 5) were grouped together as well into major damage as the accuracy assessment grouped the two classes into one. Each damage class for the UNOSAT was spatially overlain on the PGD amplification map and the value for amplification for each building extracted. The buildings were summarised based on the categorised PGD amplification. For each damage class, the PGD amplification distribution was explored using boxplot as means of characterising the damage classes with respect to amplification. Finally, the damage pattern in the study area, damage intensity map was created, in which the number of damaged buildings was divided by the number of total buildings per area (Rathje et al., 2011; WU et al., 2012). A grid size of 180m x 180m was used to develop the damage intensity map as the PGD amplification map had a resolution of 180m. The damage intensity map was compared against the classified amplification to establish the relationship between the damage pattern and PGD amplification.

## 5 RESULT

This study aimed to investigate the effects of topography on the seismic motion for the Mw 7.0 Haiti earthquake, 2010. Previous researchers have shown that topographical features may either amplify or de-amplify the seismic waves through the process of diffraction and refraction. Also, numerous studies have shown that an appropriate modelling of surface topography is necessary for effective simulation of the effect of seismic waves. In recent times, spectral element method (SEM) has been used to effectively and efficiently to simulate the effects of topography on the seismic ground motion. In this chapter, the effects of surface topography on the seismic ground motion was explored by using SEM with DEM incorporated 3D model to achieve the first specific objective. Afterwards, the findings on the relationship between ground motion with landslides and damaged building are presented to accomplish the second specific objective.

### 5.1 The Effects of Surface Topography on Seismic Ground Motion

#### 5.1.1 Mesh Design and Simulation Parameters

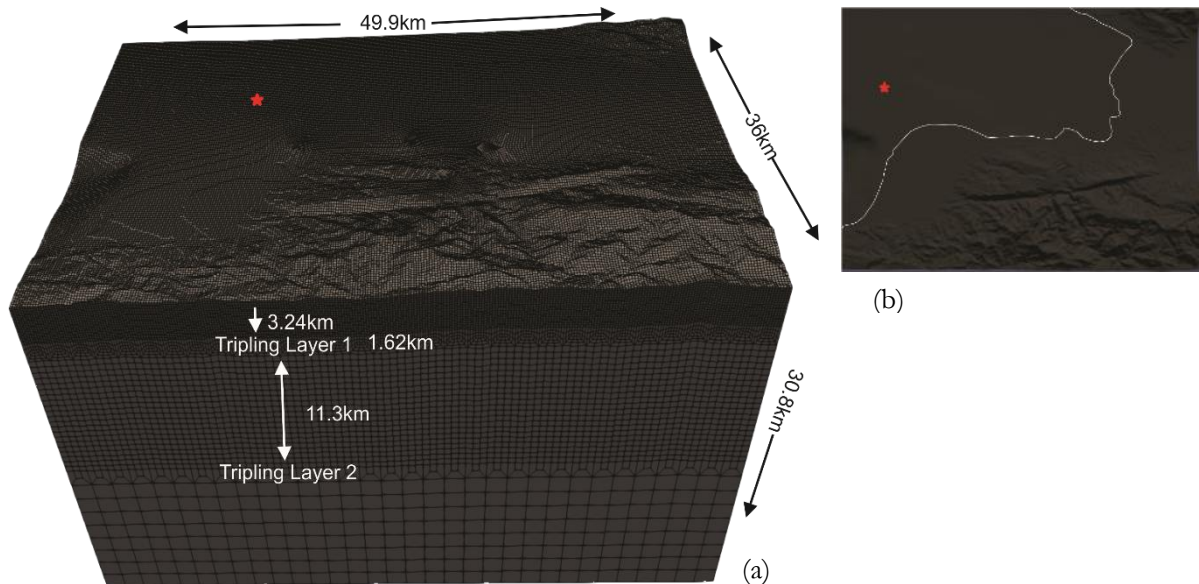


Figure 5.1 : Spectral Element Mesh, a) the mesh for Cul de Sac Basin and surrounding areas, with dimensions and location of the tripling layers. (b)The mesh surface layer with coastal boundary of Haiti (the white line) and the red star shows the CMT position which was located offshore

The designed mesh with a DEM derived surface topography incorporated in it is shown in Figure 5.1. The mesh covers an area of 49.9km x 36km with a depth of -30.8 km from + 1.9km. All the meshes were designed with two tripling layers where the elements below the tripling layer are tripled. The meshes were designed as such that the second tripling layer was below the CMT point as can be seen in Table 5.1. The second tripling layer was used to reduce the computational cost. Its location was such that there was only one tripling layer between CMT location and the surface layer.

As shown in Figure 5.2, approximate 80% mean element sizes for mesh with topography are between 128 m to 170m. The skewness in the mean element distribution was due to the use of two tripling layers. As the mesh size above the first tripling was 180, above the second tripling was 540 (m) and below that tripling layer 1620 (m). As shown in Figure 5.3 approximate 78 % of the elements in the mesh without topography had mean sizes between 165m to 201 m. As with the case mesh with topography, the skewness of the mean size distribution was due to the use two tripling layers. However, in the mesh without topography, the first mean element size shows the majority as the top layer was flat.

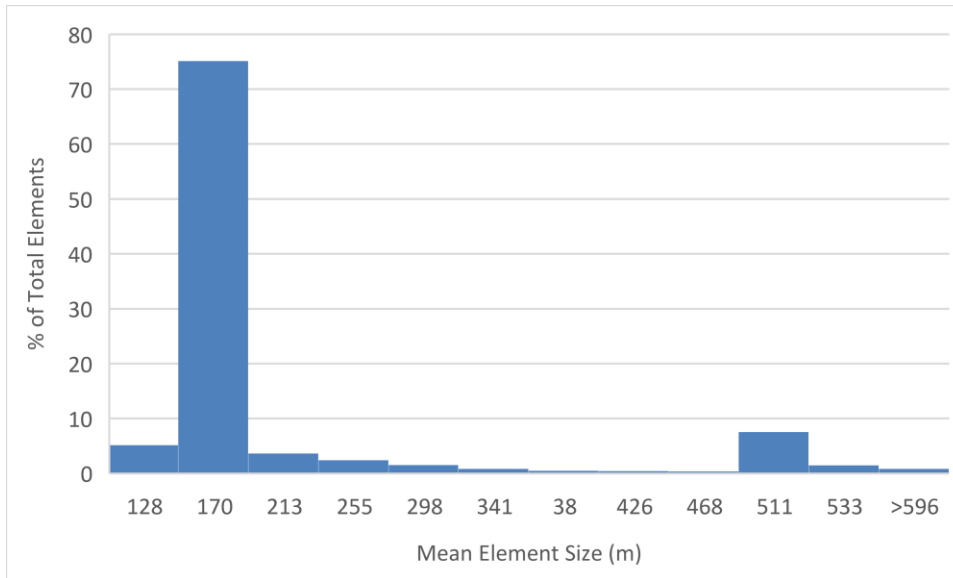


Figure 5.2 The major element size for 180m with topography

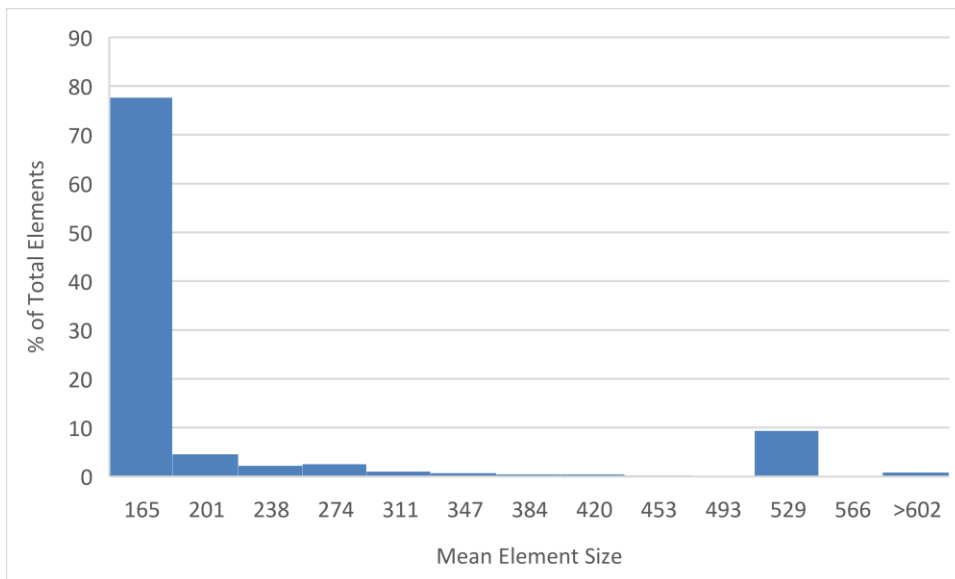


Figure 5.3: The major element size for 180m without topography

By looking at the quality of the mesh, the skewness of the elements was used to evaluate the quality of the mesh. Skewness is used to indicate how distorted the elements are in the mesh. SEM uses hexahedral elements as such elements have the faces intersecting at 90 degrees will have no distortion and skewness of

zero. But as elements become more distorted as intersecting faces changes from 90-degree, the skewness would veer toward one which is maximum distortion. The maximum skewness for the mesh with topography was 0.82. In mesh without topography, the maximum skewness value was 0.65 for 1.7 % of the elements as the top surface was flat and there was less distortion in the elements to accommodate the surface layer. In contrast, mesh with topography had a higher skewness value as the topography surface was complex and with the resolution of the mesh used, the elements were more distorted. In fact, the skewness for the mesh with topography was greater than the threshold of 0.8 recommended by Casarotti et al., (2008) but with only two elements or 0.00012% of total elements, the mesh was accepted. The presence of these skewed elements may reduce the accuracy of the simulation for the mesh with topography, but with a minute quantity, the effects may be negligible. Also, the skew elements were located mainly below the mountainous region and in the tripling layers. Furthermore, none of these elements were noted to be among the surface elements.

The mesh characteristics are shown in Table 5.1 for the mesh with topography and without topography. For the mesh with topography, the total number of elements were 1.44 million, and the mesh without topography was 1.42 million. In addition, mesh with topography is also shown to have a higher degree of freedom (DOF) which is due to it having a higher number of elements. As shown in Table 5.1, the mesh with topography was the more computational expensive with very small elements located within that model than the mesh without topography. The computational cost is expressed by the length of each time step which is a function of element size and seismic wave speed. The length of time step for each model shown in Table 5.1 was chosen after an initial simulation run in SPEC3D which calculate the maximum length of time step needed for stability of the simulation

Table 5.1: Mesh (180m) properties for seismic simulation

Mesh and Simulation Properties	Mesh	Mesh (flat surface topography)
Dimension (km <sup>3</sup> )	49.9x36 x (30.8 +1.9)	49.9x36x30.8
Depth of first tripling (km)	3.24	3.24
Depth of second tripling (km)	16.2	16.2
Depth of CMT (km)	12	12
Total number of elements (millions)	1.44	1.42
Maximum GLL distance (m)	710.96	549.13
Minimum GLL distance (m)	4.67	23.31
Maximum element size	2171.83	1677.38
Minimum element size	27.22	135
Number of grid points (million)	94.3	93.9
Number of degree of freedom (million)	283	278.8
MPI process (CPUs)	32	32
Simulation time (s)	50	50
Number of time step	250,000	100,000
Length of each time step	0.0002	0.0005

Time taken for complete simulation (hours: minutes)	128:46	32:41
--	--------	-------

The mesh with topography was able to resolve seismic waves with a period of 0.754 sec (i.e., up to a frequency of 1.33 Hz) and without topography period of 0.582 sec were resolved (i.e., up to a frequency of 1.72 Hz).

If we now turn to the simulation process, mesh with topography was processed within 128 hrs 46 minutes across 32 cores by decompressing the mesh into 32 slices as shown by the message passing interface (MPI) in Table 5.1. The number of time steps for this model was 250,000 for a 50 seconds simulation, the length of time step was 0.0002. The number of time step for the mesh without topography was a quarter of the 180m mesh with topography and was processed in 32hrs 41minutes across 32 cores

### 5.1.2 Peak Ground Motion Pattern

The ground motion indicators obtained after the seismic wave simulation are shown in Figure 5.4 (a) and (b) as peak ground displacement maps more the model with topography and the model without topography respectively. As shown in Figure 5.4a, the seismic waves can be seen to be modified by the surface topography as compared with the situation in Figure 5.4b, which results in amplification or de-amplification as shown in Figure 5.4d. The maximum displacement observed based on the mesh with topography inland was in the coastal area of the Léogâne delta with an approximate displacement of 20 m. The displacement values in Cul de Sac basin was around 75 cm to 140 cm in the central region of the basin. At the basin edge, displacement was approximately 350 cm to 400 cm as there are small hills around Petion Ville. as shown the Figure 5.4c and Figure 5.14.

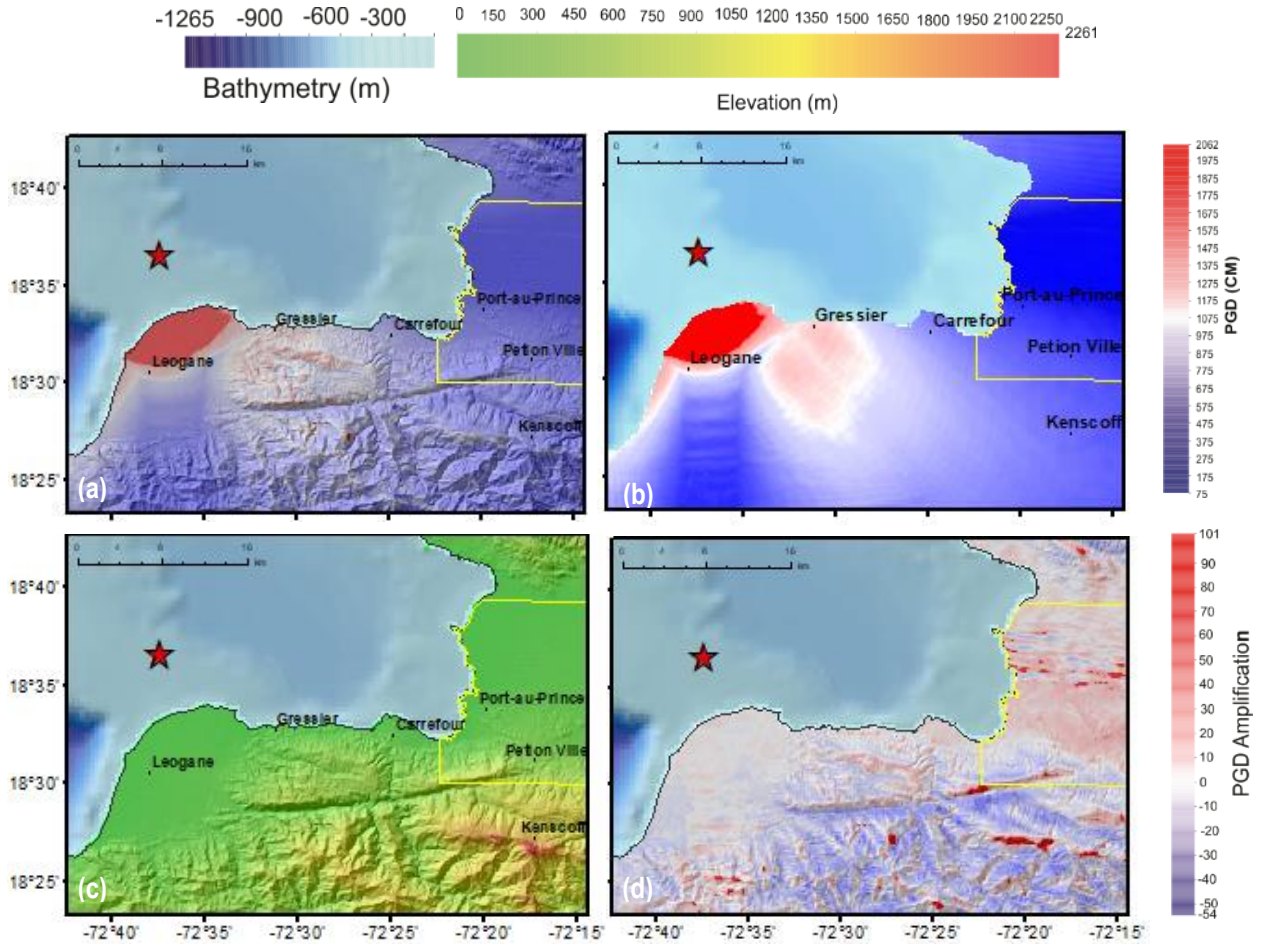


Figure 5.4: Peak Ground Displacement (PGD) Model (a) PGD for model with topography, (b) PGD for model without topography, (c) Surface topography (DEM), (d) PGD amplification (%) in which red colours indicate amplification. The blue and white colours indicate deamplification and little to no amplification respectively. The red star indicates the CMT location. The Cul-de-Sac Basin and boundary hills are indicated by the yellow line which includes the capital city, Port-au-Prince.

### 5.13 Displacement in the wavefield with time

The shake movie for the Z component of the displacement wavefield of the 2010 7.0 Mw Haiti earthquake is shown in Figure 5.5. As shown in the Figures 5.5 (b - d), the seismic wavefield was modified by the surface topography. In Figure 5.5(c), the parts of the wavefield is slows down as indicated by the black triangle due to topography and the blue arrow indicates parts of the wavefield that is not restricted by topography.

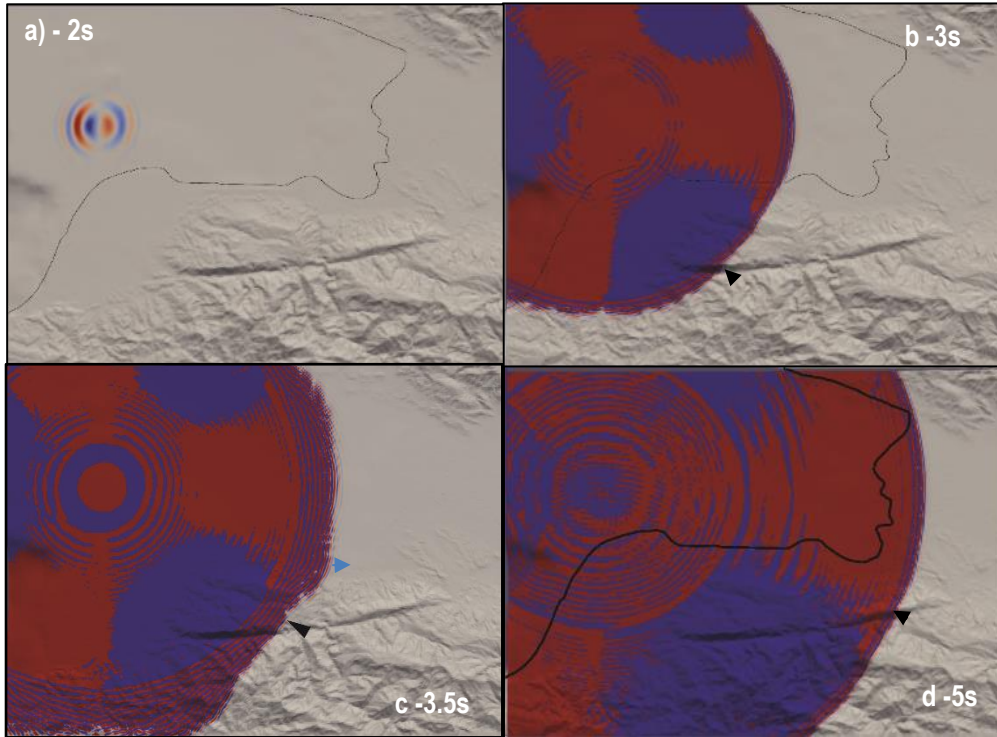


Figure 5.5: Snapshots at different time steps for the Z-component displacement wavefield of the 2010 Haiti earthquake propagating across the surface (A-d). Red colours denote positive values and blue negative values. Wavefield distortions are due to topographic effects as shown by the back triangle and the blue arrow shows where wavefield was less distorted.

#### 5.1.4 Seismogram analysis

Several artificial seismic stations were placed across the study area as shown in Figure 5.6, with the seismic station at Presa de Sabaneta, Dominican Republic (SDDR). The SDDR station is about 108 km away from the artificial station 2 and approximately 147 km away from the CMT point

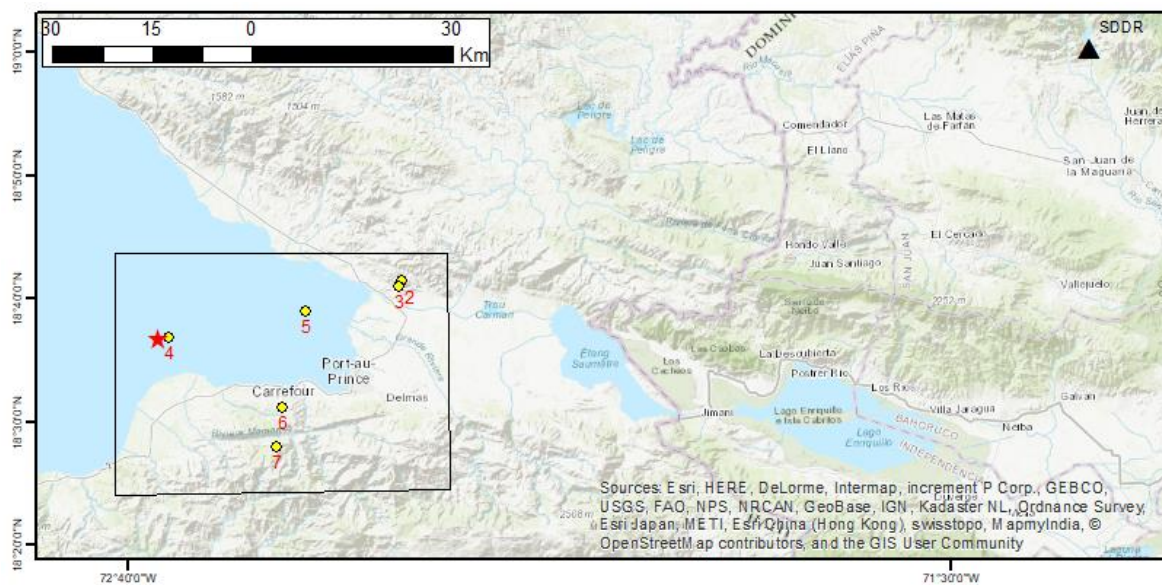


Figure 5.6: The location of the seismic station in Presa de Sabaneta, Dominican Republic with station name – SDDR (black triangle), the CMT location (red star), the artificial seismic station (yellow circles – labeled 2-7) and the study area (black box).

The synthetic seismogram obtained artificial stations were plotted and stacked together with the closest station to CMT point at the base and the station that is farthest plotted on top as shown in Figure 5.6. As there were no research seismograph stations in Haiti, the seismograms were stack as to test if the model is simulating the seismic event. As can be seen in Figure 5.7, the migration of the first seismic wave from about 1 second to about 8 seconds was an indication of the movement of the seismic waves from CMT to the farthest artificial seismic station. The comparisons of the seismograms from the artificial signal with the observed seismic signal are presented in Figure 5.8

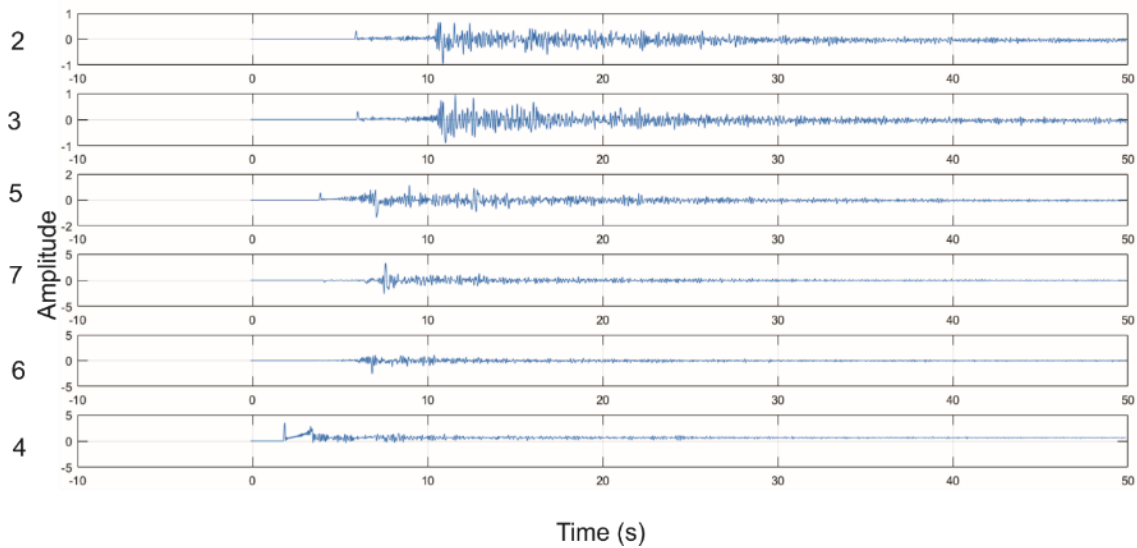


Figure 5.7: Comparison of the artificial seismograms, the z component is presented in each case.

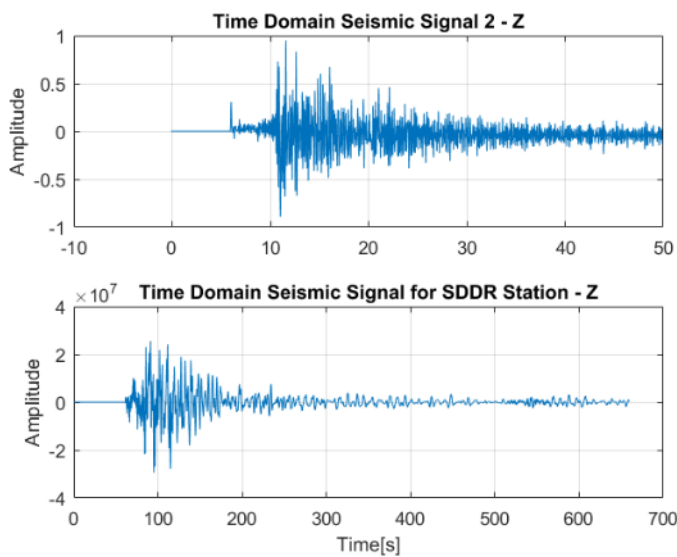


Figure 5.8: Comparison of the observed (SDDR) signal with the signal from station 2, a) shows the time difference between the two signals

### 5.2 Relation Between Landslides and Seismic Amplification

The landslides points (3872) were generated from the Gorum et al. (2013) landslide inventory and is shown in Figure 5.9, where polygon data had been transformed into point data and spatial overlain on the PGD amplification map.

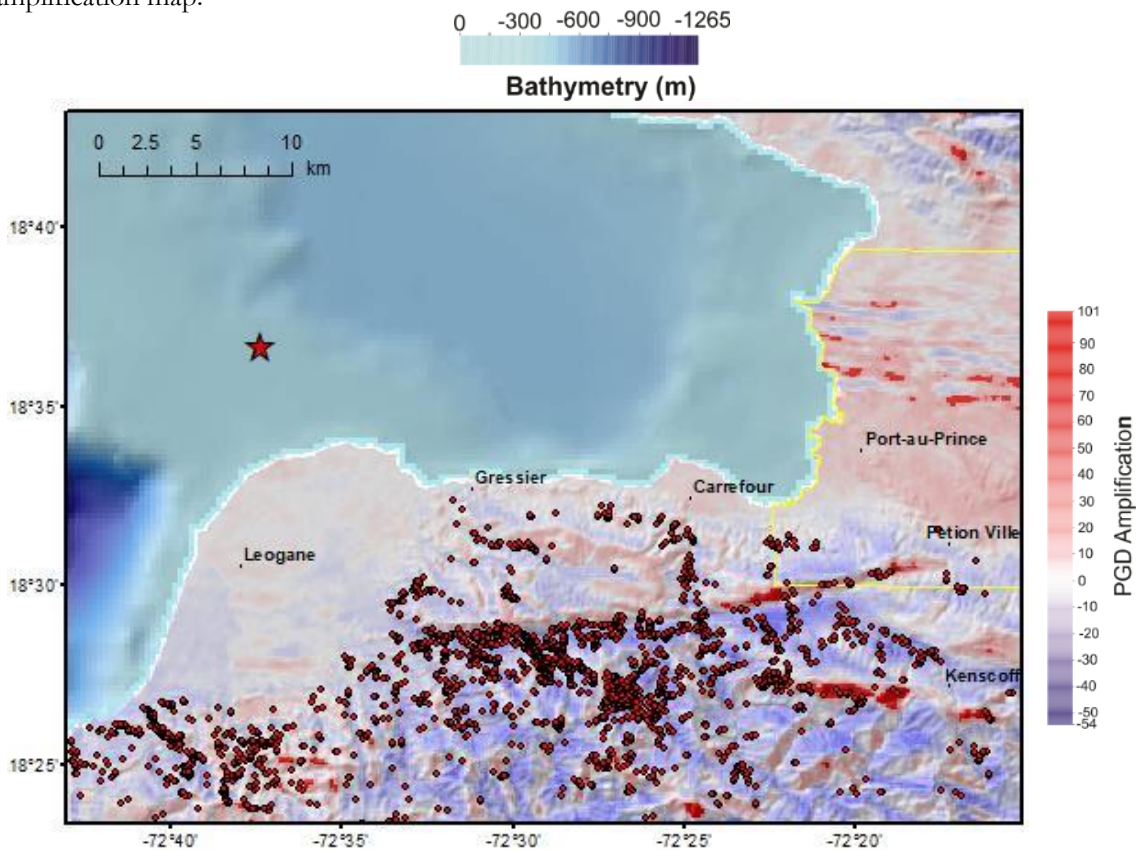


Figure 5.9: Landslides (red dots) located within study area along with the CMT.

The Figures 5.9 shows that was a complex relationship with landslides and amplification as a large number of landslides were located in the areas that the models predicted to have deamplification as can be seen in Table 5.2 below. The amplification values have been categorised as shown in Table 5.2. The extracted landslides and corresponding amplification values have been summarised in the Table 5.2. What stands out in the Table 5.2 is that the largest number of landslides were located in areas that have been moderately deamplified with 1947 landslides.

Table 5.2: Landslides and Amplification Maps with classified amplification

		PGD Amplification	Number of landslide
Amplification / Deamplification	High Amplification	>40	30
	Moderate Amplification	40< amp >10	505
	Low Amplification	10< amp >0	547
	Low Deamplification	0 < amp > -10	750
	Moderate Deamplification	-10 < amp > -40	1947
	High Deamplification	-40 <	93

The distribution of landslides with respect to CMT location is shown in Figure 5.10a, and the relationship between this distribution is compared with the amplification values for the landslide in Figure 5.10b. From the Figure 5.10, it can be seen that approximately 40.5% (1568) of the landslides are in a back-azimuth range of 120 to 140 from CMT. However, there is no clear pattern or strong relationship with amplification and landslides based on their azimuth from the CMT as indicated by Figure 5.10b.

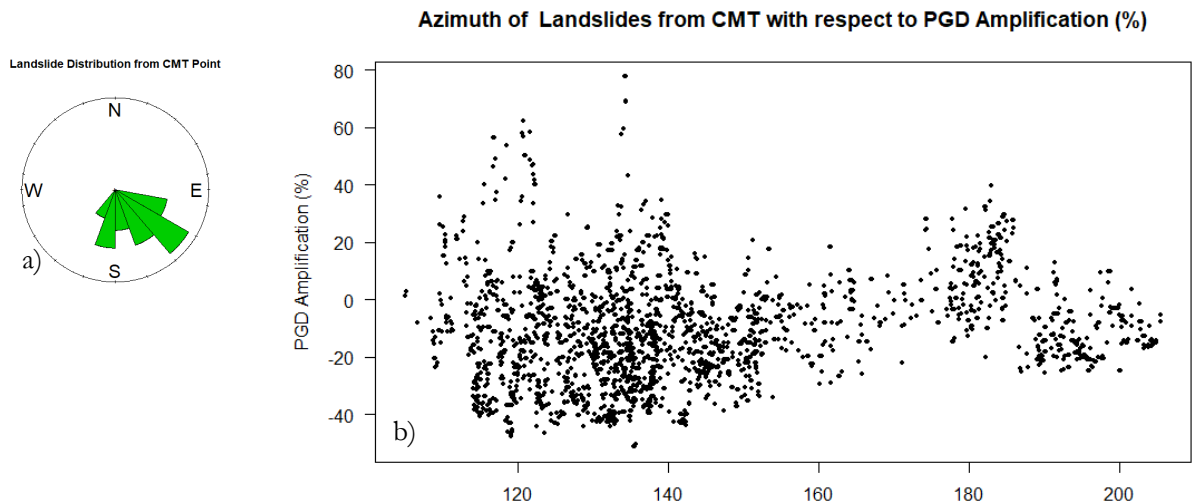


Figure 5.10: (a) shows the distribution of Landslide with respect to CMT location in a rose diagram. (B) shows back azimuth of the landslide from CMT against the PGD amplification

The landslides aspect and their corresponding PGD amplification are shown in Figure 5.11 as boxplots. Figure 5.11 shows that landslides on slopes with aspects southeast facing have a median value in the amplified zone. The slopes that are facing north, northwest, and west had approximate 75 % of landslides on the slopes that were indicated to have experienced deamplification as shown in Figure 5.11. It is observed that the pattern of amplification can be seen where the median and the third quartile of the boxplot are shown to be in the amplified zones for east, northeast, south, and southeast. This pattern of amplification for the landslides in the study area that were on the southeast facing slopes indicate that majority of these landslides were amplified. Furthermore, the amplification of the slides on southeast facing slopes more than the other aspects could be as a result of these slopes being normal to the seismic wavefield and facing away from the seismic source (the CMT). A similar observation made by a study by Meunier et al. (2008) that the landslides tend to be on slopes facing away from the earthquake source. However, there are many disparities between the amplification model and landslides distribution which could be related to scaling of the model and the scale used to map the landslides. In addition, the study area is comprised of a complex surface topography and resolution of the mesh used to capture this topography may give a good approximation of the surface. However, due to the complexity of the area there are still need to improve mesh design and increase resolution in order to obtain an appropriate amplification pattern in this area.

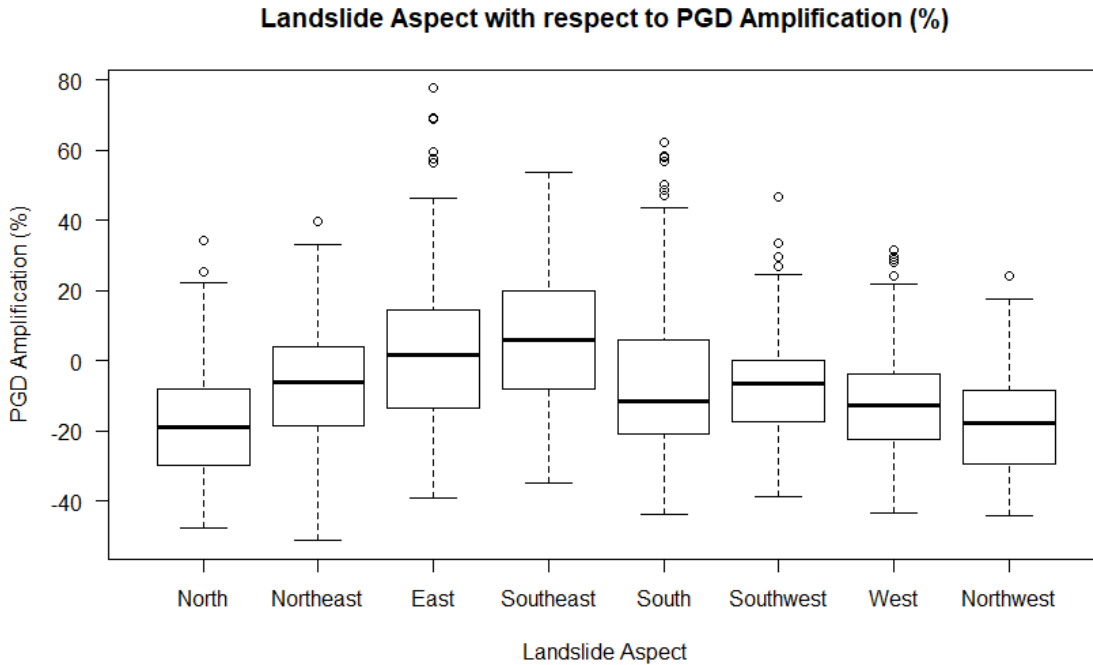


Figure 5.11: Box plot of the landslide aspect against the PGD amplification.

### 5.2.2 Normalized Landslide Density map vs Normalized Amplification Map

A normalized landslide density map was generated from the landslide point data. A landslide density map was generated by computation the percentage of landslides within a kernel of area 1km<sup>2</sup> (Gorum et al., 2011) and a pixel size of 180m based on resolution of the amplification map. The maximum landslide density is 86.4/km<sup>2</sup>. The landslide density map was normalized with respect to the highest density and classified using into density classes based on modified scheme of Gorum et al. (2011). The density classes used are high (>0.45), medium (0.1-0.45), low (0.02-0.1) and very low (<0.02) as shown in Figure 5.12.

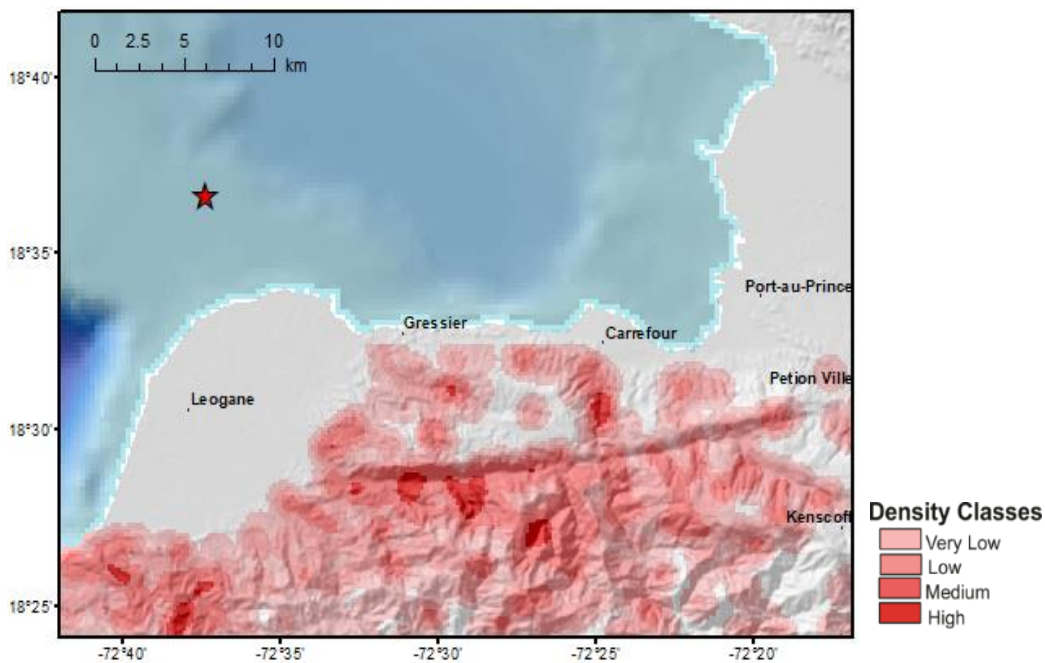


Figure 5.12: Landslide density map with density

The landslide density map is spatially overlain with the amplification to indicate the spatial distribution of amplified or deamplified landslides as shown in Figure 5.13. A clear pattern of amplified landslides can be seen on slopes that were facing away from the CMT (seismic source). However, the slopes that were facing towards the CMT tend to have deamplified landslides.

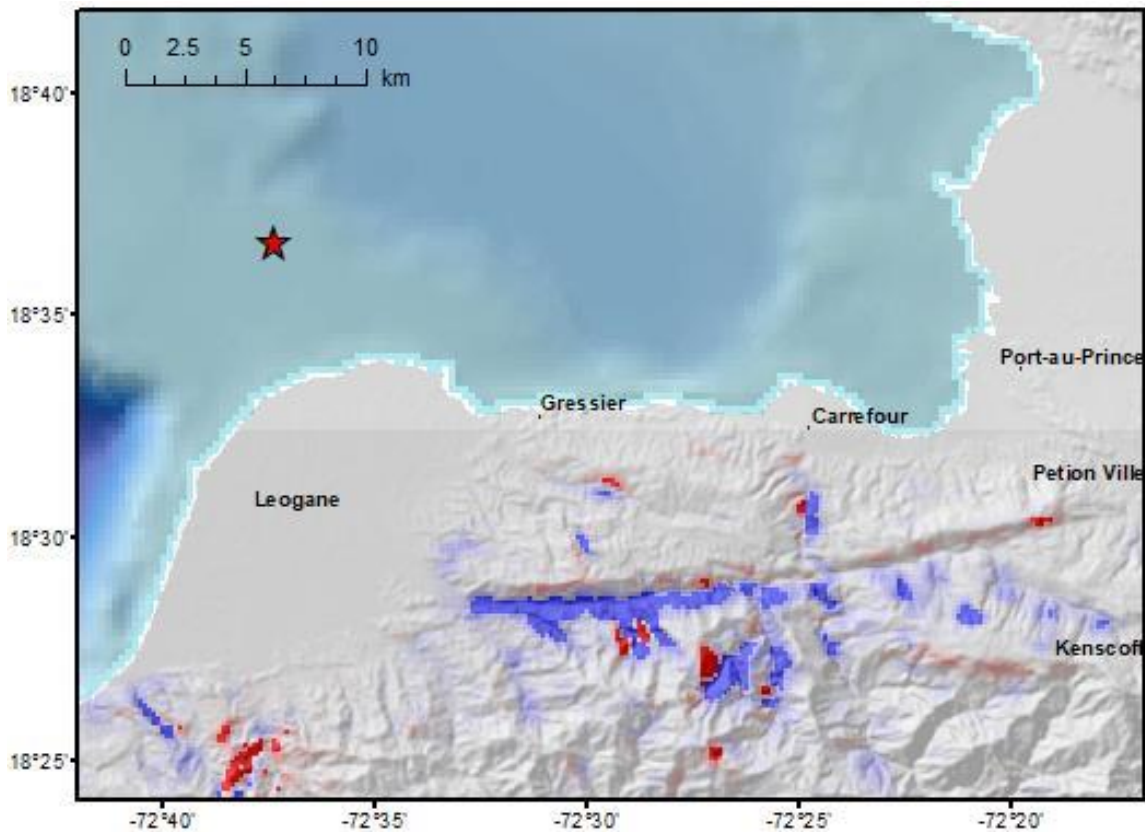


Figure 5.13: Landslide Density with respect to PGD amplification. The blue areas are landslides that were de-amplified and the red areas are landslides that were amplified. The red star indicates that CMT location.

## Relation Between Observed Building Damages and Seismic Amplification

### 5.3.1. Comparison of Amplification Model with Reference site

As shown in Figure 5.15, Hotel Montana (used as the reference site as a means to evaluate the amplification) was spatially overlain on the amplification maps and amplification value extracted. As noted in chapter 3, studies by Rathje et al. (2011); Assimaki & Jeong, (2013), and Hough et al., (2010) indicated that damages to Hotel Montana could partly be due to topography induced amplification. Therefore, the extracted amplification for Hotel Montana was used to evaluate the amplification model. The Hotel was used as a reference as there were not research seismic stations in the study area. The extracted value for Hotel Montana based on the PGD amplification model was 10%. The extracted amplification value for Hotel Montana has inferred that the PGD amplification model was capable of modelling the topographic effects in an area of low relief but very complex as shown in Figure 5.15b.

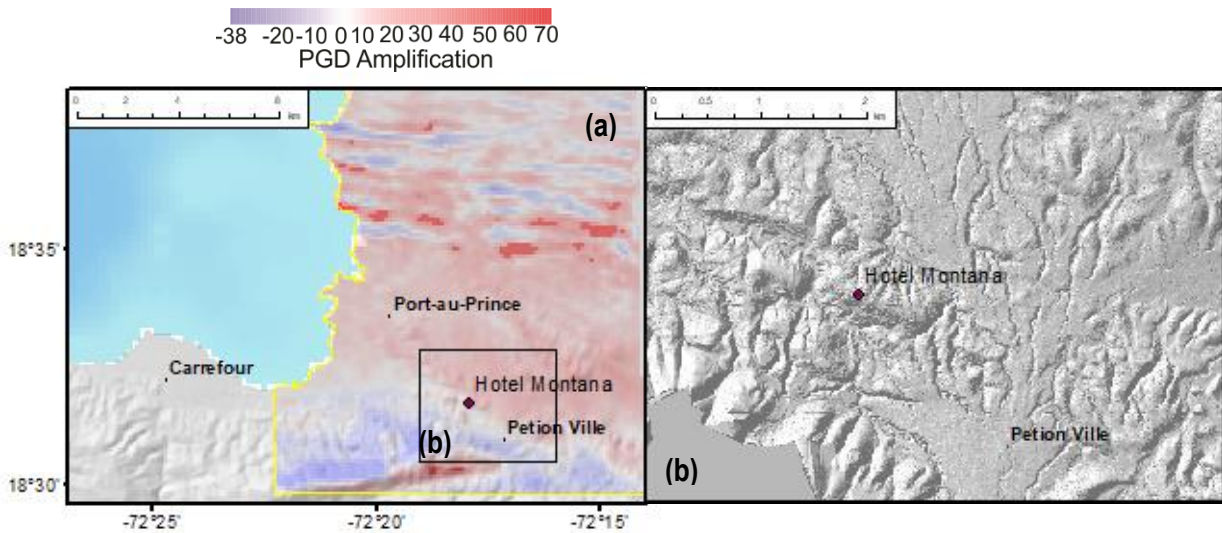


Figure 5.14: PGD amplification model with Hotel Montana (reference site – purple circle) – (a) PGD amplification model, the black box outlines the area shown in (b), the yellow outline shows the Cul de Sac region. (b) Hotel Montana (purple circle), LiDAR based hillslope model showing the complex terrain for the area where Hotel Montana is located

### 5.3.3. Damage Mapping in the Cul De Sac

The damage map for the Cul De Sac region based on the UNOSAT inventory is shown in Figure 5.18. It is seen that areas around Hotel Montana and Petion Ville, there are no damage information. The lack of damage information in those area may indicate the extent of the inventory as those areas are marked by sharp boundaries. The general damage pattern shows that in the southwestern and western section of the damage map the damage was more intense than in the other areas. The number of buildings mapped by UNOSAT within the Cul de Sac area were 170503 buildings of which 30174 (17.7%) were mapped as heavy damage buildings and the other 140329 (82.3%) buildings were mapped as no to moderate damaged buildings.

The damage map was analyzed against the amplification map to establish the relationship between the damage classes and amplification. Amplification categories used to analyses the landslides, those categories were also used to determine the amplification status of the damage classes.

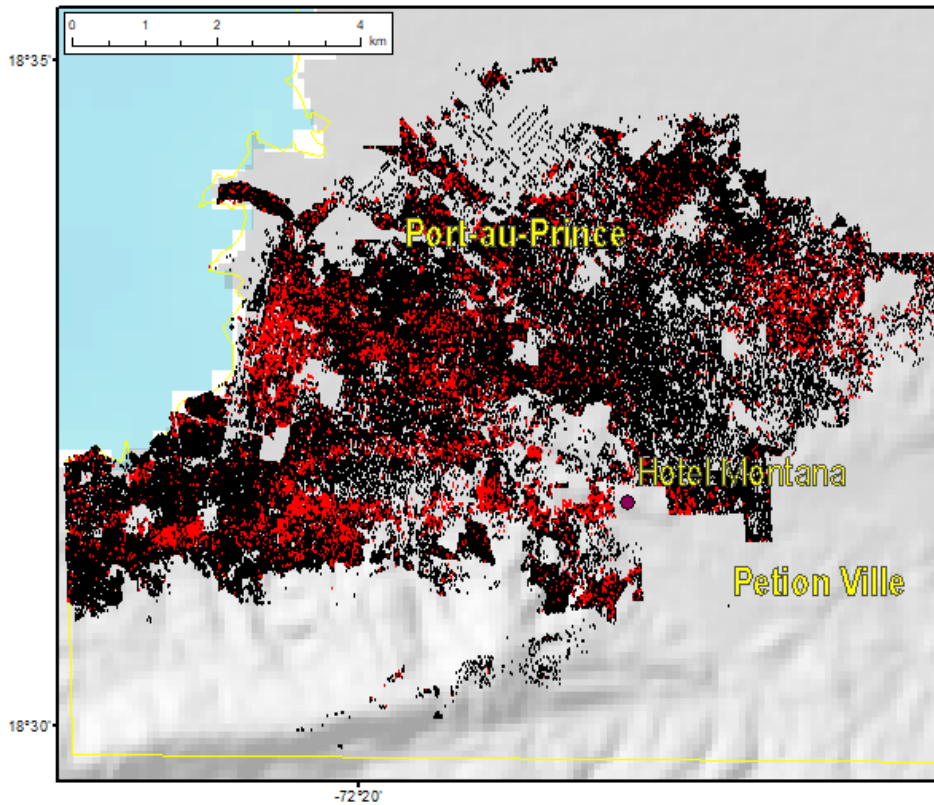


Figure 5.15: Distribution of UNOSAT inventory, red area are buildings that were classified as heavy damaged and black areas were buildings classified as no/moderate damaged.

#### 5.3.4. No/ Moderate Damage against Amplification

The no/moderate damaged buildings were spatially analyzed against the PGD amplification map as shown in Figure 5.19 and the amplification value of each building obtained. As shown in Table 5.3 a large number of the no/moderate damaged buildings amounting to 106407 were located in moderate to low amplification areas which is about 76% of the no to moderate damage buildings. It should be noted that the no to moderate classes includes buildings that were classified by UNOSAT as “Grade 3 - Substantial damage to Heavy Damage” but was incorporated into the no to moderate damage class. The grade 3 damage class is poorly classified with near nadir optical remote sense (Rathje & Adams, 2008).

Table 5.3: Number of no/moderate damaged Buildings with respect to classified PGD amplification

		PGD Amplification	Number of Buildings
Amplification / Deamplification	High Amplification	>40	0
	Moderate Amplification	40< amp >10	56290
	Low Amplification	10< amp >0	50117
	Low Deamplification	0 < amp >-10	28807
	Moderate Deamplification	-10 < amp > -40	5115
	High Deamplification	-40 <	0

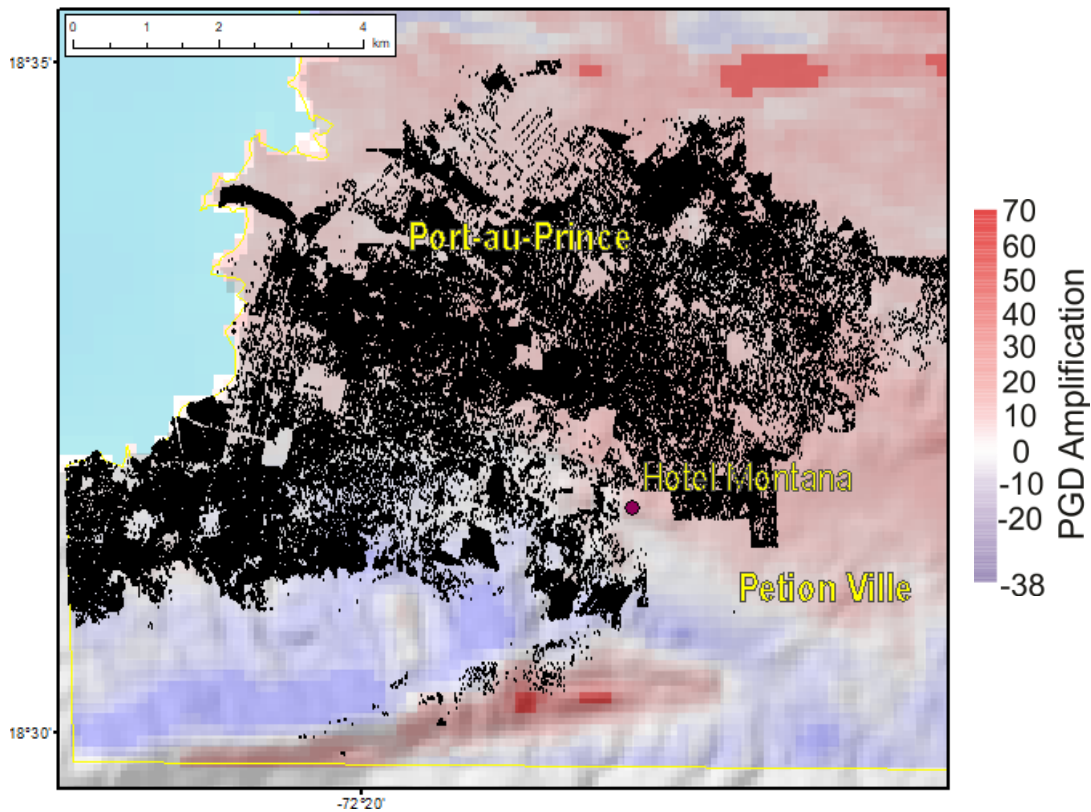


Figure 5.16: The spatial distribution of no/moderate damaged buildings with respect to PGD amplification

#### 5.3.4. Heavy Damage against Amplification

The heavy damaged buildings were spatially analyzed against the PGD amplification map as shown in Figure 5.20 and the amplification value of each building obtained. As shown in Table 5.3 a large number of the heavy damaged buildings amounting to 21738 were located in moderate to low amplification areas which is about 71% of the heavy damage buildings. However, what stands out in the table is that 8436 of heavy damaged buildings were located in areas that were classified as low deamplification to moderate deamplification which is approximately 29%.

Table 5.4: Number of heavy damaged buildings with respect to classified PGD amplification

		PGD Amplification	Number of Buildings
Amplification / Deamplification	High Amplification	>40	0
	Moderate Amplification	40 < amp > 10	9779
	Low Amplification	10 < amp > 0	11959
	Low Deamplification	0 < amp > -10	6995
	Moderate Deamplification	-10 < amp > -40	1441
	High Deamplification	-40 <	0

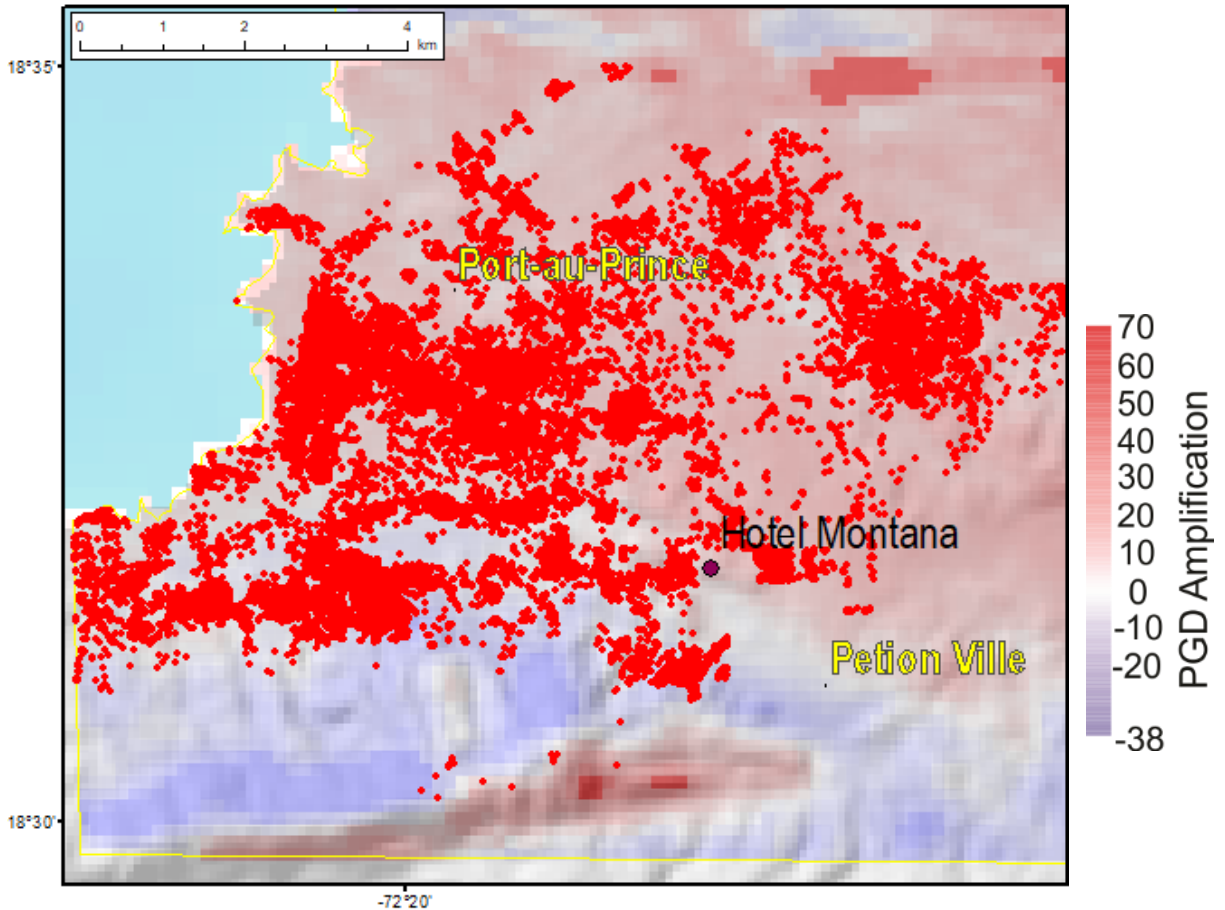


Figure 5.17: The spatial distribution of heavy damaged buildings with respect to PGD amplification

#### 5.3.4. Amplification value pattern for the two damage classes

The damages classes were plotted against amplification as boxplot as shown in Figure 5.21. What is striking about the boxplots is that both classes have relatively similar interquartile range of the amplification values. with a range value of 12.5 and 12 for no/minor damage and heavy damaged buildings respectively. This lack of trend between the two damages could be related to inclusion of the damage class 3 into the no/minor damage class. However, studies by Rathje et al. (2011); Paultre et al. (2013) and Marshall et al. (2011) have indicated the quality of the buildings in Port au Prince and surroundings were generally of poor quality with little earthquake proofing and many of the engineered buildings had little or no earthquake proofing.

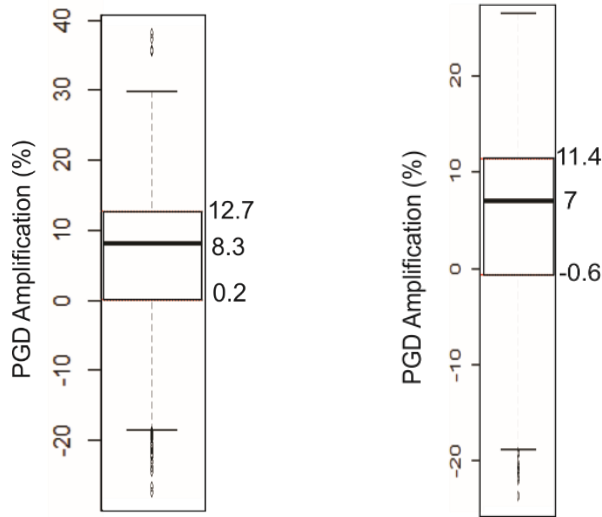


Figure 5.18: Boxplot of the amplification values for no/moderate damaged buildings (a) and heavy damaged buildings (b)

Boxplot for PGD Amplification Value Distribution for no/moderate damaged Damaged Buildings

Boxplot for PGD Amplification Value Distribution for Heavy Damaged Buildings

### 5.3.4. Damage Density Vs Amplification

As shown in Figure 5.19, the UNOSAT building inventory and the heavy damaged building data were spatially overlain grid map of 180 m x 180 m. The number of building located in each grid were used to define the total building and heavy damage building maps as shown in Figure 5.2. These were used to generate damage density map as shown in Figure 5.20. The damage density map was spatially overlain on with the PGD amplification map and the amplification value extracted. The extracted amplification values for categorized based on the categories in groups based on the amplification in Table 4.1.

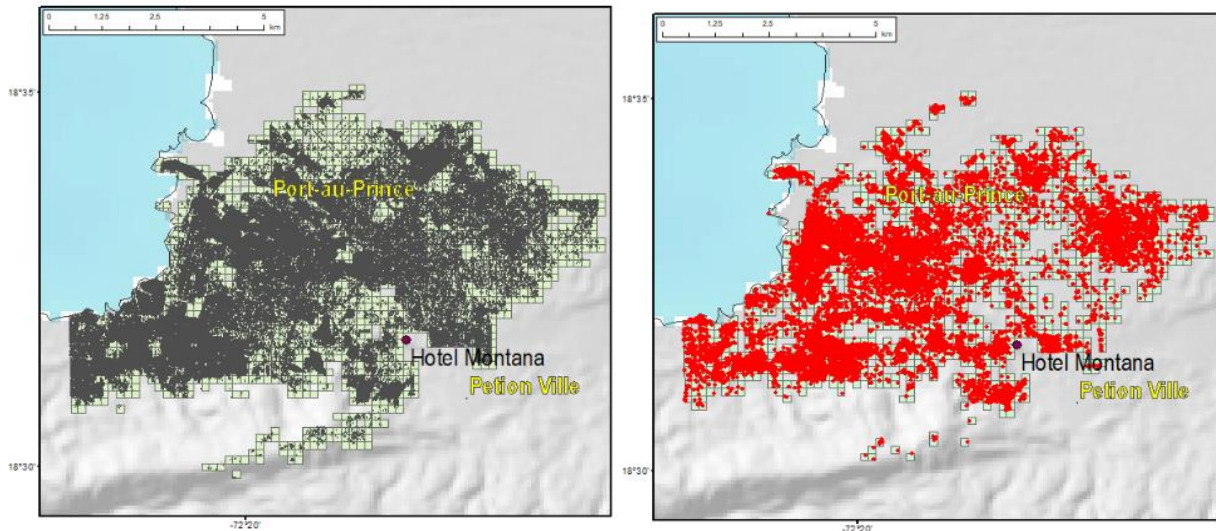


Figure 5.19: Total Building Map (a) with the buildings shown black points and the Damage Map (b) with damaged buildings as red points

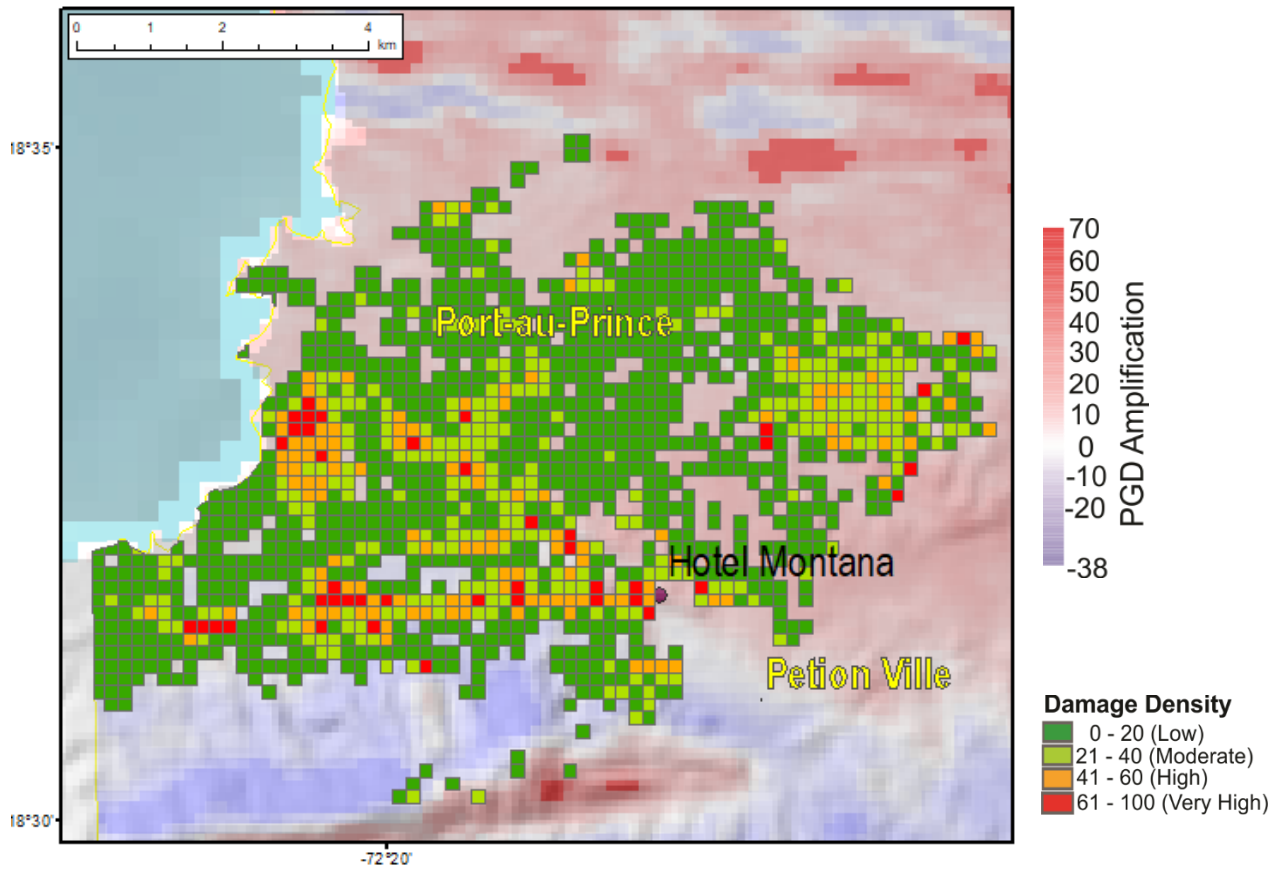


Figure 5.20: Damage Density overlain on PGA Amplification map

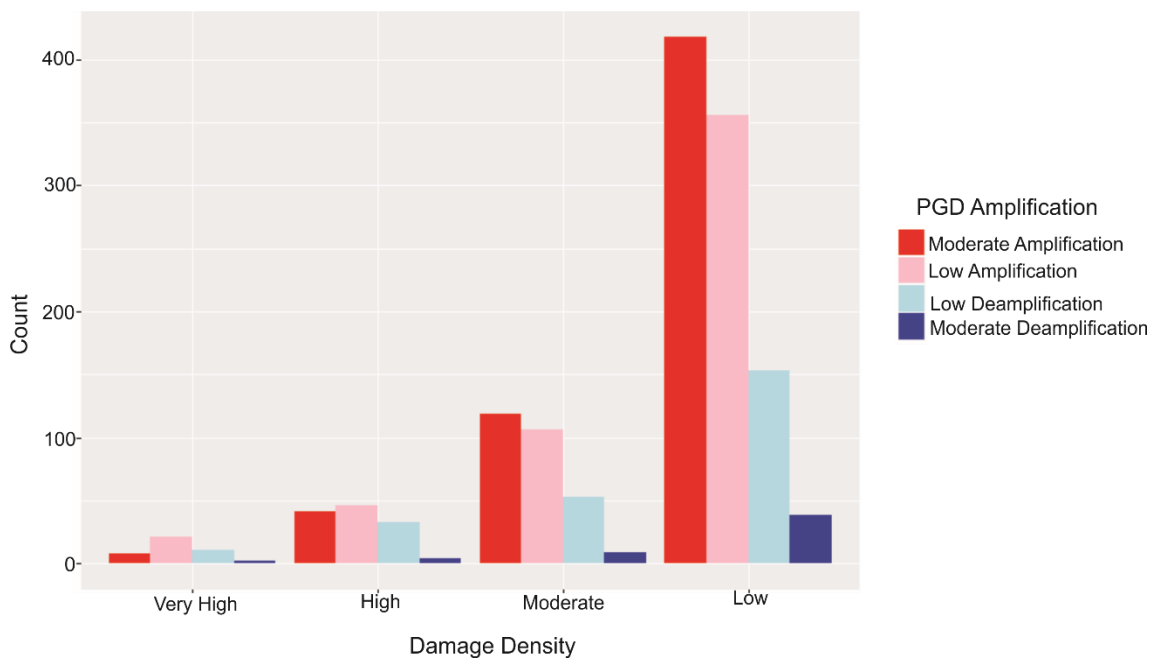


Figure 5.21: The damage density with respect to categorised PGD amplification

In Figure 5.20 and Figure 5.21, what is striking in but figures are that in the low damage density area, most of the buildings were mapped to have amplification values were low to moderate amplification. This observation may indicate that the PGD amplification model based on the effects of topography does not correlate well with the buildings in the low damage density areas. In addition, as seen in Figure 5.20, most of these low damage density areas are located in the central part of the basin. In the central part of the basin, topographic effects are less likely to play a part and sediments induced amplification may become more important. From the Figure 5.21, it is observed that areas that were mark as very high to high damaged density areas were modelled to greater extent as experiencing low amplification especially former density class.

The results presented in this chapter were based on application of the methods discussed in previous chapters. These results suggest that SEM is an effective means of evaluating the effects of topography on the seismic motion for the 2010 Mw 7.0 Haiti earthquake. The results from the earthquake simulation when compared with the landslides had provided an insight into the interaction of seismic waves with a rugged terrain which resulted in complex landslides pattern. In addition, the results from the simulation were also compared with damaged building and were presented as well. The next chapter, therefore, moves on to discuss the findings obtained.

## 6. DISCUSSION

This chapter provides a discourse about the main findings of this research as well as an examination of the limitations of the method applied and data used. The main objective of this study was to examine the effects of topography on the seismic ground motion of Mw 7.0 2010, Haiti earthquake and the associated earthquake-induced landslides and building damages.

### Mesh Design: 270m vs 180m mesh resolution

As mention in the literature review, designing the mesh is a critical and difficult stage (Casarotti et al., 2008; Komatitsch et al., 2013). In addition, deciding what is the appropriate resolution of mesh design for an area can add to the complication. However, a study by Khan et al. (2017) had suggested mesh resolution of 270m is appropriate to capture the effects of topography on seismic motion. The study by Khan et al. (2017) used an area located in the mountainous area surrounding Muzaffarabad, Pakistan but based on a single ridge crest. On the other hand, this study was located in an area with relief that shows complex geometry for its hills and mountains. To give an estimate of the of the effects of mesh resolution of 270m and mesh resolution of 180m for the study area, two models were design with only the resolution at the surface making the different in design as shown in Table 6.1. Although the mesh at 270m covers a larger area than the one at 180m, it does not affect the simulation results.

Table 6.1: Mesh design for 270m and 180m resolution

Mesh and Simulation Properties	Mesh resolution (270m)	Mesh (180m)
Dimension (km <sup>3</sup> )	66x45x30	49.9x36 x (30.8 +1.9)
Depth of 1 <sup>st</sup> tripling (km)	5.7	3.24
Depth of 2 <sup>nd</sup> tripling (km)	15.4	16.2
Depth of CMT (km)	12	12
Total number of elements (millions)	0.985	1.44
Maximum GLL distance (m)	1091.83	710.96
Minimum GLL distance (m)	14.72	4.67
Maximum element size	3335.75	2171.83
Minimum element size	85.24	27.22
Number of grid points (million)	64.8	94.3
Number of degree of freedom (million)	194.5	283
MPI process (CPUs)	44	32
Simulation time (s)	50	50
Number of time step	52000	250,000
Length of each time step	0.0009	0.0002
Time taken for complete simulation (hours: minutes)	11:59	128:46

The simulated results were plotted and are shown in Figure 6.1 For the 180m resolution mesh, the amplification changes are sharper and less intense in general (Figure 6.2b) however, in some areas the amplification is very large as on the top of Massif de la Sella (Figure 6.1a). Khan et al. (2017) indicated that higher amplification intensities were associated a coarser resolution mesh model than for the finer resolution mesh model as there is less scattering of the seismic waves. The coarsening of the mesh model results in smoothing as indicated by Shafique et al.(2011) due to DEM aggregation especially with the relief features that are less than the aggregated DEM resolution results smoothing effects. The large amplification for the 270m mesh tends to be in the gullies or on the hillside and not necessary on the top of the ridges (Figure 6.1b). Poursartip et al. (2017) indicated that changes in topographic features due to the representation model of the terrain may result in change in amplification pattern and location of the maxima as shown in Figure 6.1 and Figure 6.2.

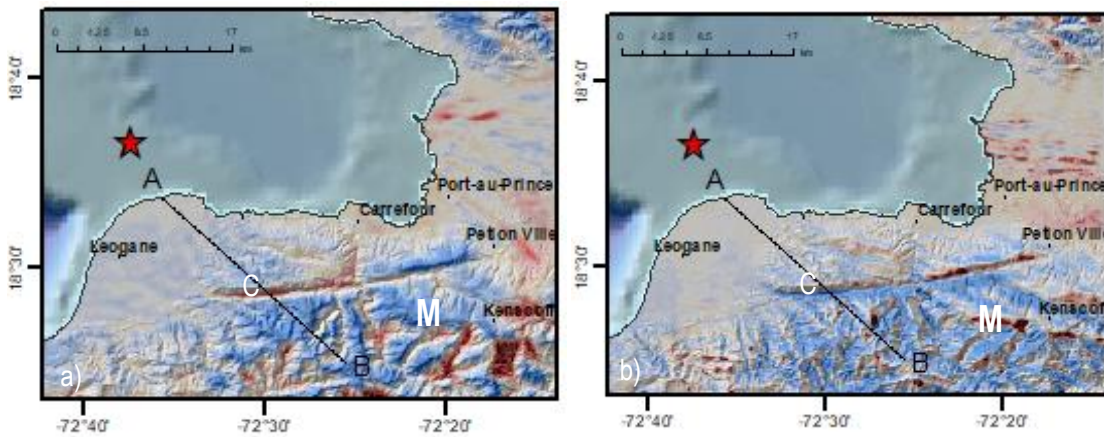


Figure 6.1: PGD amplification model: a) 270m resolution, b) 180m resolution. The profile A-B which is shown in Figure 6.2, C is position at 13km on the profile indicated as the blue line in Figure 6.2, M- Massif de la Sella

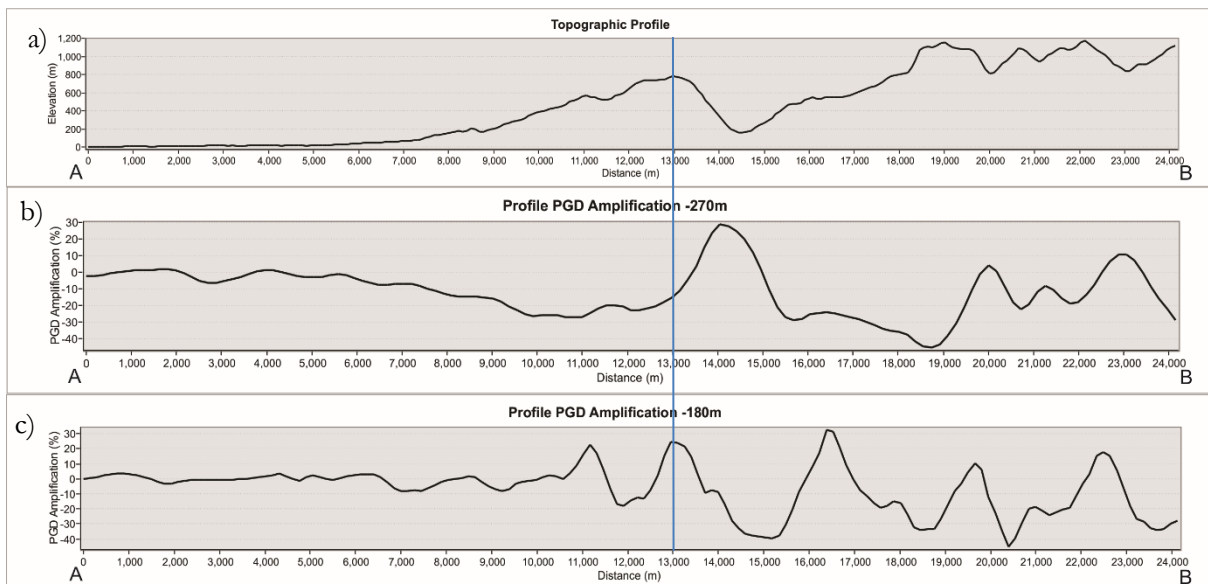


Figure 6.2: Profile A-B: a) topographic profile, b) PGD Amplification -270m model, c) PGD Amplification -180m model. The blue line indicated the same position across the profiles mark as C in Figure 6.1

Additionally, an increase in mesh resolution had resulted an increase in a complexity in amplification pattern. A similar result was made by Lee et al. (2009), who had used a mesh model that incorporate a surface models based 40m DEM and 1m DTM.

### Landslide and Amplification

The landslide density can be very useful when combined with the amplification model, highlighting how amplification relates to landslide density and as such how much of the landslides are due to terrain features in conjunction with seismic forcing from an earthquake. Meunier et al., (2008) indicated that slope failure tends to be more on the hill slope facings away from the seismic source. This pattern was somewhat observed but could not explain most of the landslides in the study area. Gorum et al. (2013) indicated that possible the complex rupture dynamics and topography primary control the pattern of landslides. The resolution used for the modelling could not indicated that topography was a major contributor as shown in Figure 6.3 and 6.4. It indicated that some landslides are associated with amplification but a majority of them were associated with deamplification based on this association topography features could not be major role in landslide pattern as indicated by the model.

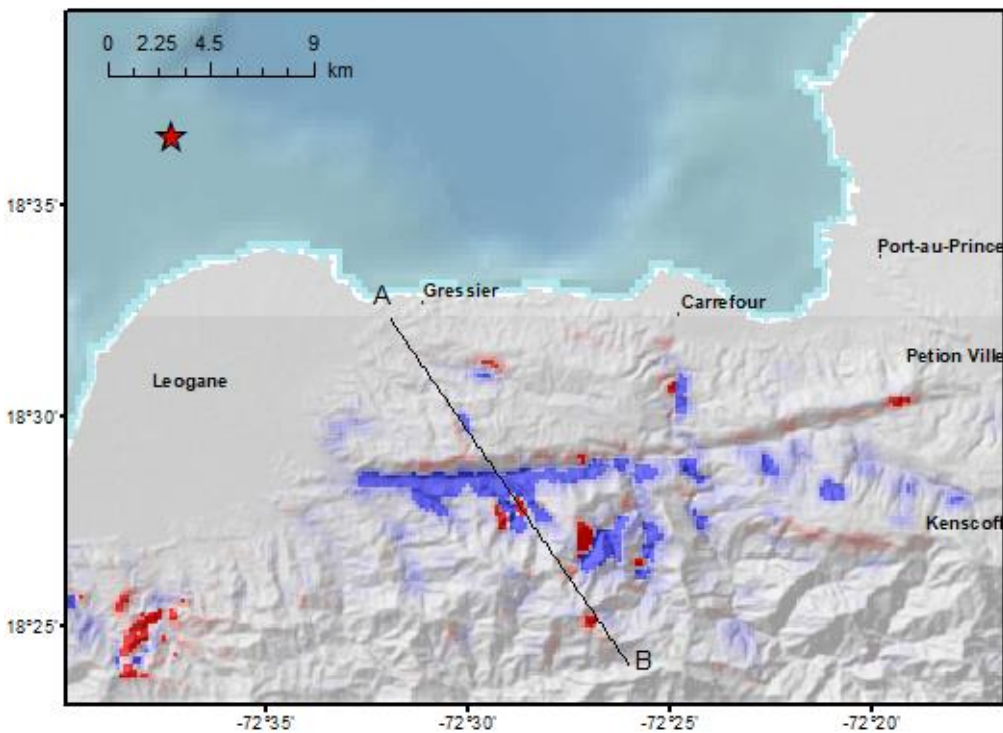


Figure 6.3: PGD amplification landslide density map. A-B profile line for Figure 6.4

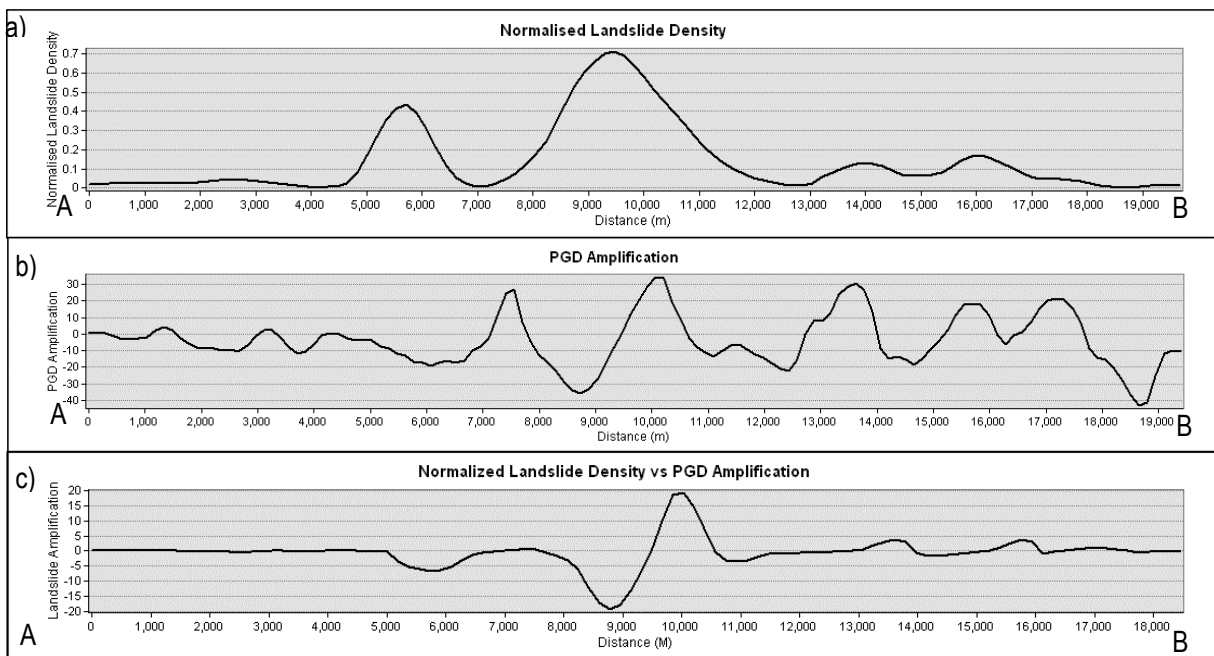


Figure 6.4: 5Profile A:B PGD amplification landslide density, a) normalized landslide density, b) PGD amplification, c) PGD amplification landslide density.

#### Amplification with Building Damage

As noted above, the PGD mesh model was able to capture small topographic details that were associated with foot slopes of Massif de la Sella. St Fleur et al. (2016) indicated that Port-au-Prince is situated on the foot hills of Massif de la Sella which shows complex topography. The damage density around Port-au-Prince area. varies considerable with very high damage density area next to low damage density area. This may be as result of affluent neighborhoods are juxtaposed poor neighborhoods as such relating damage density pattern with amplification becomes complicated. Rathje et al. (2011) made a similar observation in their study of damage patterns in Port-au-Prince during the 2010 Haiti earthquake, however, the study was more of an observation and quality study. The comparison of damage density with PGD amplification have indicated that a large number of the areas that were significantly damage experienced low PGD amplification. It gives an indication that the quality of house may be a significant factor in the damage pattern as indicated by studies by Marshall et al., (2011) and Paultre et al., (2013). It should be noted that the lack of building vulnerability data and the lack of measured ground motion data for the study area limits this study but the study highlights the need for getting building vulnerability data.

## 7. CONCLUSION

The main goal of the present research was to examine the effects of topography on the seismic motion of the 2010 7.0 Mw Haiti earthquake. The earthquake resulted in numerous damaged buildings in several towns, including the capital Port-au-Prince which is situated at the edge of the Cul-de-Sac basin. In addition, numerous landslides were generated in the surrounding hills of the Cul-de-Sac basin. The research used Spectral Element Method (SEM) to simulate the seismic event through the finite element mesh as a means to generate ground motion map. The study has confirmed that SEM is a powerful tool for simulating the effects of topography on the seismic motion for the Haiti earthquake

In addition to modelling the effects of topography on the seismic motion, the second aim of the study was to investigate the models' ability to elucidate the spatial bias in the occurrence of landslides and damaged buildings in the study area due to 2010 7.0 Mw Haiti earthquake. The relationship between landslide pattern and the PGD amplification was very complex and topographic amplification as indicated by the simulated model could not explain the majority of the landslides. In examining the relationship between damaged buildings and PGD amplification. The study has found that using damage density along with PGD amplification provides a means of understanding the damage distribution. In light of the lack of building vulnerability data and no ground motion data, this study indicates that amplified ground motion along with construction practices may have played a major role in the damage distribution.

This study indicates that in areas where topography features are small using a fine resolution mesh of 180m or less can provide an insight how topography induced amplification played a role in damaged building distribution. However, in landslides studies, in area of complex terrain, the question raised by this study what is optimal mesh resolution that is best of capturing earthquake landslides distribution. Further research might explore this question of optimal mesh resolution for regions like Haiti that experienced spatial bias in earthquake induced landslides.

## REFERENCES

- Ashrafuzzaman, M., & MD. (2017). *Surface Topography Effects on Seismic Ground Motion and Correlation with Building Damages during the 2015 Mw 7.8 Nepal Earthquake (Msc. Thesis)*. University of Twente. Retrieved from <https://www.mendeley.com/research-papers/surface-topography-effects-seismic-ground-motion-correlation-building-damages-during-2015-mw-7-8-nep/>
- Assimaki, D. (2005). Effects of Local Soil Conditions on the Topographic Aggravation of Seismic Motion: Parametric Investigation and Recorded Field Evidence from the 1999 Athens Earthquake. *Bulletin of the Seismological Society of America*, 95(3), 1059–1089. <https://doi.org/10.1785/0120040055>
- Assimaki, D., & Jeong, S. (2013). Ground-Motion Observations at Hotel Montana during the M 7.0 2010 Haiti Earthquake: Topography or Soil Amplification? *Bulletin of the Seismological Society of America*, 103(5), 2577–2590. <https://doi.org/10.1785/0120120242>
- Blacker, T., Owen, S. J., Staten, M. L., Quadros, R. W., Hanks, B., Clark, B., ... Showman, S. (2016). *CUBIT: Geometry and Mesh Generation Toolkit 15.2 User Documentation*. Retrieved from [https://cubit.sandia.gov/public/15.2/help\\_manual/Printed\\_Documentation/Cubit\\_15.2\\_User\\_Documentation.pdf](https://cubit.sandia.gov/public/15.2/help_manual/Printed_Documentation/Cubit_15.2_User_Documentation.pdf)
- Booth, E., Saito, K., Spence, R., Madabhushi, G., & Eguchi, R. T. (2011). Validating assessments of seismic damage made from remote sensing. *Earthquake Spectra*, 27(SUPPL. 1), S157–S177. <https://doi.org/10.1193/1.3632109>
- Calais, E., Freed, A., Mattioli, G., Amelung, F., Jónsson, S., Jansma, P., ... Momplaisir, R. (2010). Transpressional rupture of an unmapped fault during the 2010 Haiti earthquake. *Nature Geoscience*, 3(11), 794–799. <https://doi.org/10.1038/ngeo992>
- Casarotti, E., Stupazzini, M., Lee, S. J., Komatitsch, D., Piersanti, A., & Tromp, J. (2008). CUBIT and Seismic Wave Propagation Based Upon the Spectral-Element Method: An Advanced Unstructured Mesher for Complex 3D Geological Media. In *Proceedings of the 16th International Meshing Roundtable* (pp. 579–597). Berlin, Heidelberg: Springer Berlin Heidelberg. [https://doi.org/10.1007/978-3-540-75103-8\\_32](https://doi.org/10.1007/978-3-540-75103-8_32)
- Çelebi, M. (1991). Topographical and geological amplification: case studies and engineering implications. *Structural Safety*, 10(1–3), 199–217. [https://doi.org/10.1016/0167-4730\(91\)90015-2](https://doi.org/10.1016/0167-4730(91)90015-2)
- CIG. (2015). *COMPUTATIONAL INFRASTRUCTURE FOR GEODYNAMICS (CIG): SPECFEM 3D Cartesian*. Retrieved from <https://geodynamics.org/cig/software/specfem3d/specfem3d-manual.pdf>
- Corbane, C., Saito, K., Dell’Oro, L., Bjorgo, E., Gill, S. P. D., Emmanuel Piard, B., ... Eguchi, R. T. (2011). A Comprehensive Analysis of Building Damage in the 12 January 2010 Mw7 Haiti Earthquake Using High-Resolution Satellite and Aerial Imagery. *Photogrammetric Engineering & Remote Sensing*, 77(10), 997–1009. <https://doi.org/10.14358/PERS.77.10.0997>
- Corbeau, J., Rolandone, F., Leroy, S., Guerrier, K., Keir, D., Stuart, G., ... Meyer, B. (2017). Crustal structure of western Hispaniola (Haiti) from a teleseismic receiver function study. *Tectonophysics*, 709, 9–19. <https://doi.org/10.1016/J.TECTO.2017.04.029>
- Cupillard, P., Delavaud, E., Burgos, G., Festa, G., Vilotte, J. P., Capdeville, Y., & Montagner, J. P. (2012). RegSEM: A versatile code based on the spectral element method to compute seismic wave propagation at the regional scale. *Geophysical Journal International*, 188(3), 1203–1220. <https://doi.org/10.1111/j.1365-246X.2011.05311.x>
- DeMets, C., Jansma, P. E., Mattioli, G. S., Dixon, T. H., Farina, F., Bilham, R., ... Mann, P. (2000). GPS geodetic constraints on Caribbean-North America plate motion. *Geophysical Research Letters*, 27(3), 437–440. <https://doi.org/10.1029/1999GL005436>
- DesRoches, R., Comerio, M., Eberhard, M., Mooney, W., & Rix, G. J. (2011). Overview of the 2010 Haiti Earthquake. *Earthquake Spectra*, 27(S1), S1–S21. <https://doi.org/10.1193/1.3630129>
- Dhanya, J., Maheshreddy Gade, @bullet, Raghukanth, @bullet S T G, & Raghukanth, S. T. G. (2017). Ground motion estimation during 25th April 2015 Nepal earthquake. *Acta Geodaetica et Geophysica*, 52, 69–93. <https://doi.org/10.1007/s40328-016-0170-8>
- Douilly, R., Ellsworth, W. L., Kissling, E., Freed, A. M., Deschamps, A., & Mercier de Lépinay, B. (2016). 3-D velocity structure in southern Haiti from local earthquake tomography. *Journal of Geophysical Research: Solid Earth*, 121(12), 8813–8832. <https://doi.org/10.1002/2016JB013123>
- Douilly, R., Haase, J. S., Ellsworth, W. L., Bouin, M. P., Calais, E., Symithe, S. J., ... Hough, S. E. (2013). Crustal structure and fault geometry of the 2010 Haiti earthquake from temporary seismometer deployments. *Bulletin of the Seismological Society of America*, 103(4), 2305–2325.

- <https://doi.org/10.1785/0120120303>
- Ekström, G., Nettles, M., & Dziewoński, A. M. (2012). The global CMT project 2004–2010: Centroid-moment tensors for 13,017 earthquakes. *Physics of the Earth and Planetary Interiors*, 200–201, 1–9. <https://doi.org/10.1016/J.PEPI.2012.04.002>
- European Commission-Joint Research Centre, United Nations Institute for Training and Research-Operational Satellite Applications Program, World Bank-Global Facility for Disaster Reduction and Recovery, C. N. d'Information G.-S. (2010). *Building Damage Assessment Report Post Disaster Needs Assessment and Recovery Framework (PDNA) Distribution record*.
- Fichtner, A. (2011a). *Full Seismic Waveform Modelling and Inversion*. Berlin, Heidelberg: Springer Berlin Heidelberg. <https://doi.org/10.1007/978-3-642-15807-0>
- Fichtner, A. (2011b). Spectral-Element Methods (pp. 59–81). [https://doi.org/10.1007/978-3-642-15807-0\\_4](https://doi.org/10.1007/978-3-642-15807-0_4)
- Fletcher, J. B., Spudich, P., & Baker, L. M. (2006). Observations at the UPSAR. *Bulletin of the Seismological Society of America Rupture Propagation*, 96(4B), 129–142. <https://doi.org/10.1785/0120050812>
- Gerke, M., & Kerle, N. (2011). Automatic Structural Seismic Damage Assessment with Airborne Oblique Pictometry© Imagery. *Photogrammetric Engineering & Remote Sensing*, 77(9), 885–898. <https://doi.org/10.14358/PERS.77.9.885>
- Gorum, T., Fan, X., van Westen, C. J., Huang, R. Q., Xu, Q., Tang, C., & Wang, G. (2011). Distribution pattern of earthquake-induced landslides triggered by the 12 May 2008 Wenchuan earthquake. *Geomorphology*, 133(3–4), 152–167. <https://doi.org/10.1016/J.GEOMORPH.2010.12.030>
- Gorum, T., Van Westen, C. J., Korup, O., van der Meijde, M., Fan, X., & Van Der Meer, F. D. (2013). Complex rupture mechanism and topography control symmetry of mass-wasting pattern, 2010 Haiti earthquake. *Geomorphology*, 184, 127–138. <https://doi.org/10.1016/j.geomorph.2012.11.027>
- Grünthal, G. (1998). *European Macroseismic Scale 1998. European Center of Geodynamics and ...* (Vol. 15). Hough, S. E., Altidor, J. R., Anglade, D., Given, D., Janvier, M. G., Maharrey, J. Z., ... Yong, A. (2010). Localized damage caused by topographic amplification during the 2010 M 7.0 Haiti earthquake. *Nature Geoscience*, 3(11), 778–782. <https://doi.org/10.1038/ngeo988>
- Hough, S. E., Taniguchi, T., & Altidor, J. R. (2012). Estimation of peak ground acceleration from horizontal rigid body displacement: A case study in Port-au-Prince, Haiti. *Bulletin of the Seismological Society of America*, 102(6), 2704–2713. <https://doi.org/10.1785/0120120047>
- Ishii, M., Shearer, P. M., Houston, H., & Vidale, J. E. (2005). Extent, duration and speed of the 2004 Sumatra-Andaman earthquake imaged by the Hi-Net array. *Nature*, 435(7044), 933–936. <https://doi.org/10.1038/nature03675>
- Kerle, N. (2013). Remote Sensing Based Post-Disaster damage mapping. In S. Zlatanova, R. Peters, A. Dilo, & H. Scholten (Eds.), *Intelligent Systems for Crisis Management* (pp. 121–133). Berlin, Heidelberg: Springer Berlin Heidelberg. [https://doi.org/10.1007/978-3-642-33218-0\\_9](https://doi.org/10.1007/978-3-642-33218-0_9)
- Khan, S., van der Meijde, M., van der Werff, H., & Shafique, M. (2017). Impact of Mesh and DEM Resolutions in SEM Simulation of 3D Seismic Response. *Bulletin of the Seismological Society of America*, 107(5), 2151–2159. <https://doi.org/10.1785/0120160213>
- Komatitsch, D., Liu, Q., Tromp, J., Süß, P., Stidham, C., & Shaw, J. H. (2004). Simulations of Ground Motion in the Los Angeles Basin Based upon the Spectral-Element Method. *Bulletin of the Seismological Society of America*, 94(1), 187–206. <https://doi.org/10.1785/0120030077>
- Komatitsch, D., Tromp, J., & Sciences, P. (1999). Introduction to the spectral element method for three-dimensional seismic wave propagation. *Geophys. J. Int.*, 139, 806–822.
- Komatitsch, D., Tromp, J., & Vilotte, J.-P. J. (1998). The spectral element method for elastic wave equations: Application to 2D and 3D seismic problems. In *SEG Technical Program Expanded Abstracts 1998* (pp. 1460–1463). Society of Exploration Geophysicists. <https://doi.org/10.1190/1.1820185>
- Komatitsch, D., Tsuboi, S., & Tromp, J. (2013). The Spectral-Element Method in Seismology. *Seismic Earth: Array Analysis of Broadband Seismograms*, 205–227. <https://doi.org/10.1029/157GM13>
- Komatitsch, D., & Vilotte, J.-P. (1998). The Spectral Element Method : An Efficient Tool to Simulate the Seismic Response of 2D and 3D Geological Structures. *Bulletin of the Seismological Society of America*, 88(2), 368–392. Retrieved from <http://dx.doi.org/>
- Lee, S.-J. J., Liu, Q., Tromp, J., Komatitsch, D., Liang, W.-T. T., & Huang, B.-S. S. (2014). Toward real-time regional earthquake simulation II: Real-time Online earthquake Simulation (ROS) of Taiwan earthquakes. *Journal of Asian Earth Sciences*, 87, 56–68. <https://doi.org/10.1016/J.JSEAES.2014.02.009>
- Lee, S.-J. S. J. S.-J., Chen, H.-W. H. C., Liu, Q., Komatitsch, D., Huang, B. S. B.-S., & Tromp, J. (2008).

- Three-dimensional simulations of seismic-wave propagation in the Taipei Basin with realistic topography based upon the spectral-element method. *Bulletin of the Seismological Society of America*, 98(1), 253–264. <https://doi.org/10.1785/0120070033>
- Lee, S. J., Chan, Y. C., Komatitsch, D., Huang, B. S., & Tromp, J. (2009). Effects of realistic surface topography on seismic ground motion in the Yangminshan region of Taiwan based upon the spectral-element method and LiDAR DTM. *Bulletin of the Seismological Society of America*, 99(2 A), 681–693. <https://doi.org/10.1785/0120080264>
- Lee, S. J., Komatitsch, D., Huang, B. S., & Tromp, J. (2009). Effects of topography on seismic-wave propagation: An example from Northern Taiwan. *Bulletin of the Seismological Society of America*, 99(1), 314–325. <https://doi.org/10.1785/0120080020>
- Lee, V. W., & Cao, H. (1989). Diffraction of SV Waves by Circular Canyons of Various Depths. *Journal of Engineering Mechanics*, 115(9), 2035–2056. [https://doi.org/10.1061/\(ASCE\)0733-9399\(1989\)115:9\(2035\)](https://doi.org/10.1061/(ASCE)0733-9399(1989)115:9(2035))
- Lemoine, G., Corbane, C., Louvrier, C., & Kauffmann, M. (2013). Intercomparison and validation of building damage assessments based on post-Haiti 2010 earthquake imagery using multi-source reference data. *Natural Hazards and Earth System Sciences Discussions*, 1(2), 1445–1486. <https://doi.org/10.5194/nhessd-1-1445-2013>
- Lew, M., Naeim, F., Huang, S. C., Lam, H. K., & Carpenter, L. D. (2000). The significance of the 21 September 1999 Chi-Chi earthquake, Taiwan, for tall buildings. *The Structural Design of Tall Buildings*, 9(2), 67–72. [https://doi.org/10.1002/\(SICI\)1099-1794\(200005\)9:2<67::AID-TAL144>3.0.CO;2-L](https://doi.org/10.1002/(SICI)1099-1794(200005)9:2<67::AID-TAL144>3.0.CO;2-L)
- Madariaga, R. (2007). Seismic Source Theory. In *Treatise on Geophysics* (pp. 59–82). Elsevier. <https://doi.org/10.1016/B978-044452748-6.00061-4>
- Magnoni, F., Casarotti, E., Michelini, A., Piersanti, A., Komatitsch, D., Peter, D., & Tromp, J. (2014). Spectral-element simulations of seismic waves generated by the 2009 L'Aquila earthquake. *Bulletin of the Seismological Society of America*, 104(1), 73–94. <https://doi.org/10.1785/0120130106>
- Manaker, D. M., Calais, E., Freed, A. M., Ali, S. T., Przybylski, P., Mattioli, G., ... de Chabaliér, J. B. (2008). Interseismic Plate coupling and strain partitioning in the Northeastern Caribbean. *Geophysical Journal International*, 174(3), 889–903. <https://doi.org/10.1111/j.1365-246X.2008.03819.x>
- Mann, P., Draper, G., & Lewis, J. F. (1991). An overview of the geologic and tectonic development of Hispaniola. In *Geological Society of America Special Papers* (Vol. 262, pp. 1–28). <https://doi.org/10.1130/SPE262-p1>
- Mann, P., Taylor, F. W. W., Edwards, R. L. L., & Ku, T.-L. (1995). Actively evolving microplate formation by oblique collision and sideways motion along strike-slip faults: An example from the northeastern Caribbean plate margin, 246, 1–69. [https://doi.org/10.1016/0040-1951\(94\)00268-E](https://doi.org/10.1016/0040-1951(94)00268-E)
- Marshall, J. D., Lang, A. F., Baldrige, S. M., & Popp, D. R. (2011). Recipe for Disaster: Construction Methods, Materials, and Building Performance in the January 2010 Haiti Earthquake. *Earthquake Spectra*, 27(S1), S323–S343. <https://doi.org/10.1193/1.3637031>
- Massa, M., Barani, S., & Lovati, S. (2014). Overview of topographic effects based on experimental observations: meaning, causes and possible interpretations. *Geophysical Journal International Geophys. J. Int*, 197, 1537–1550. <https://doi.org/10.1093/gji/ggt341>
- Massa, M., Lovati, S., & Barani, S. (2012). Seismic amplification in presence of topography and their consequences for ground motion predictions and seismic code for building: the case of Italy. *15th World Conference on Earthquake Engineering (15WCEE)*.
- Mercier de Lépinay, B., Deschamps, A., Klingelhoefer, F., Mazabraud, Y., Delouis, B., Clouard, V., ... St-Louis, M. (2011). The 2010 Haiti earthquake: A complex fault pattern constrained by seismologic and tectonic observations. *Geophysical Research Letters*, 38(22), n/a-n/a. <https://doi.org/10.1029/2011GL049799>
- Meunier, P., Hovius, N., & Haines, A. J. (2007). Regional patterns of earthquake-triggered landslides and their relation to ground motion. *Geophysical Research Letters*, 34(20), L20408. <https://doi.org/10.1029/2007GL031337>
- Meunier, P., Hovius, N., & Haines, J. A. (2008). Topographic site effects and the location of earthquake induced landslides. *Earth and Planetary Science Letters*, 275(3–4), 221–232. <https://doi.org/10.1016/J.EPSL.2008.07.020>
- Moczo, P., Bystrický, E., Kristek, J., Carcione, J. M., & Bouchon, M. (1997). Hybrid Modeling of P-SV Seismic Motion at Inhomogeneous Viscoelastic Topographic Structures. *Bulletin of the Seismological Society of America*, 87(5), 1305–1323.
- Nettles, M., & Hjörleifsdóttir, V. (2010). Earthquake source parameters for the 2010 January Haiti main

- shock and aftershock sequence. *Geophysical Journal International*, 183(1), 375–380.  
<https://doi.org/10.1111/j.1365-246X.2010.04732.x>
- Patera, A. T. (1984). A spectral element method for fluid dynamics: Laminar flow in a channel expansion. *Journal of Computational Physics*, 54(3), 468–488. [https://doi.org/10.1016/0021-9991\(84\)90128-1](https://doi.org/10.1016/0021-9991(84)90128-1)
- Paultre, P., Calais, É., Proulx, J., Prépetit, C., & Ambroise, S. (2013). Damage to engineered structures during the 12 January 2010, Haiti (Léogâne) earthquake 1. *Canadian Journal of Civil Engineering*, 40(8), 777–790. <https://doi.org/10.1139/cjce-2012-0247>
- Pedersen, H., Le Brun, B., Hatzfeld, D., Campillo, M., & Bard, P.-Y. (1994). Ground-Motion Amplitude Across Ridges. *Bulletin of the Seismological Society of America*, 84(6), 1786–1800.
- Peter, D., Komatitsch, D., Luo, Y., Martin, R., Le Goff, N., Casarotti, E., ... Tromp, J. (2011). Forward and adjoint simulations of seismic wave propagation on fully unstructured hexahedral meshes. *Geophysical Journal International*, 186(2), 721–739. <https://doi.org/10.1111/j.1365-246X.2011.05044.x>
- Poursartip, B., Fathi, A., & Kallivokas, L. F. (2017). Seismic wave amplification by topographic features: A parametric study. *Soil Dynamics and Earthquake Engineering*, 92(July 2016), 503–527.  
<https://doi.org/10.1016/j.soildyn.2016.10.031>
- Rathje, E. M., & Adams, B. J. (2008). The Role of Remote Sensing in Earthquake Science and Engineering: Opportunities and Challenges. *Earthquake Spectra*, 24(2), 471–492.  
<https://doi.org/10.1193/1.2923922>
- Rathje, E. M., Bachhuber, J., Dulberg, R., Cox, B. R., Kottke, A., Wood, C., ... Rix, G. (2011). Damage Patterns in Port-au-Prince during the 2010 Haiti Earthquake. *Earthquake Spectra*, 27(S1), S117–S136.  
<https://doi.org/10.1193/1.3637056>
- Saint Fleur, N., Feuillet, N., Grandin, R., Jacques, E., Weil-Accardo, J., & Klinger, Y. (2015). Seismotectonics of southern Haiti: A new faulting model for the 12 January 2010 M7.0 earthquake. *Geophysical Research Letters*, 42(23), 10273–10281. <https://doi.org/10.1002/2015GL065505>
- Shafique, M., van der Meijde, M., Kerle, N., & van der Meer, F. (2011). Impact of DEM source and resolution on topographic seismic amplification. *International Journal of Applied Earth Observation and Geoinformation*, 13(3), 420–427. <https://doi.org/10.1016/j.jag.2010.09.005>
- Snieder, R. (1986). The influence of topography on the propagation and scattering of surface waves. *Physics of the Earth and Planetary Interiors* 226–241 Elsevier Science Publishers B.V., 44. Retrieved from <https://inside.mines.edu/~rsnieder/Snieder86PEPI.pdf>
- Spudich, P., Hellweg, M., & Lee, W. H. K. (1996). Directional topographic site response at Tarzana observed in aftershocks of the 1994 Northridge, California, earthquake: Implications for mainshock motions. *Bulletin of the Seismological Society of America*, 86(1 SUPPL. B), 193–208. Retrieved from [http://usgsprojects.org/lee/Spudich\\_Hellweg\\_Lee\\_BSSA1996.pdf](http://usgsprojects.org/lee/Spudich_Hellweg_Lee_BSSA1996.pdf)
- St Fleur, S., Bertrand, E., Courboux, F., Mercier de Lépinay, B., Deschamps, A., Hough, S., ... Prépetit, C. (2016). Site Effects in Port-au-Prince (Haiti) from the Analysis of Spectral Ratio and Numerical Simulations. *Bulletin of the Seismological Society of America*, 106(3), 1298–1315.  
<https://doi.org/10.1785/0120150238>
- Suwandana, E., Kawamura, K., Sakuno, Y., Kustiyanto, E., & Raharjo, B. (2012). Evaluation of ASTER GDEM2 in Comparison with GDEM1, SRTM DEM and Topographic-Map-Derived DEM Using Inundation Area Analysis and RTK-dGPS Data. *Remote Sens*, 4, 2419–2431.  
<https://doi.org/10.3390/rs4082419>
- Taniguchi, T., & Miwa, T. (2007). A simple procedure to approximate slip displacement of freestanding rigid body subjected to earthquake motions. *Earthquake Engineering & Structural Dynamics*, 36(4), 481–501. <https://doi.org/10.1002/eqe.639>
- Trifunac, M. D. (1972). Scattering of plane sh waves by a semi-cylindrical canyon. *Earthquake Engineering & Structural Dynamics*, 1(3), 267–281. <https://doi.org/10.1002/eqe.4290010307>
- Trifunac, M. D., & Hudson, D. E. (1971). Analysis of the Pacoima dam accelerogram—San Fernando, California, earthquake of 1971. *Bulletin of the Seismological Society of America*, 61(5), 1393–1411. Retrieved from <http://dx.doi.org/>
- Tromp, J., Komatitsch, D., & Liu, Q. (2008). Spectral-element and adjoint methods in seismology. *Communications in Computational Physics*, 3(1), 1–32. Retrieved from <https://authors.library.caltech.edu/9615/1/TROccp08.pdf>
- Upreti, P., & Yamazaki, F. (2012). Use of high-resolution SAR intensity images for damage detection from the 2010 Haiti earthquake. In *2012 IEEE International Geoscience and Remote Sensing Symposium* (Vol. 12, pp. 6829–6832). IEEE. <https://doi.org/10.1109/IGARSS.2012.6352595>
- Ural, S., Hussain, E., Kim, K., Fu, C.-S., & Shan, J. (2011). Building Extraction and Rubble Mapping for

City Port-au-Prince Post-2010 Earthquake with GeoEye-1 Imagery and Lidar Data. *Photogrammetric Engineering & Remote Sensing*, 77(10), 1011–1023. <https://doi.org/10.14358/PERS.77.10.1011>

Wong, H. L., & Trifunac, M. D. (1974). Surface Motion of a Semi-Elliptical Alluvial Valley for Incident Plane Sh Waves. *Bulletin of the Seismological Society of America*, 64(5), 1389–1408. Retrieved from <http://citeseerx.ist.psu.edu/viewdoc/download?doi=10.1.1.526.8249&rep=rep1&type=pdf>

WU, H., MASAKI, K., IRIKURA, K., SAGUCHI, K., KURAHASHI, S., & WANG, X. (2012). Relationship between Building Damage Ratios and Ground Motion Characteristics during the 2011 Tohoku Earthquake. *Journal of Natural Disaster Science*, 34(1), 59–78. <https://doi.org/10.2328/jnds.34.59>